AERODYNAMICS OF KRUGER FLAP EQUIPPED AIRFOILS

By

Ken Thomson

B. A.Sc (Physics), Queen's University

A THESIS SUBMITTED IN PARTIAL FULFILLMENT OF

THE REQUIREMENTS FOR THE DEGREE OF

MASTER OF APPLIED SCIENCE

in

THE FACULTY OF GRADUATE STUDIES

MECHANICAL ENGINEERING

We accept this thesis as conforming

to the required standard

THE UNIVERSITY OF BRITISH COLUMBIA

November 1996

In presenting this thesis in partial fulfilment of the requirements for an advanced degree at the University of British Columbia, I agree that the Library shall make it freely available for reference and study. I further agree that permission for extensive copying of this thesis for scholarly purposes may be granted by the head of my department or by his or her representatives. It is understood that copying or publication of this thesis for financial gain shall not be allowed without my written permission.

Mechanical Engineering

The University of British Columbia

2075 Wesbrook Place

Vancouver, Canada

V6T 1Z1

Date:

November 5, 1996

Abstract

The pressure distributions along two airfoil models of differing profiles equipped with upper surface Kruger flaps were measured. The results were compared with the predictions of a theoretical potential flow model, which used conformal mapping to bring the flapped airfoils into a final transform plane where the profile of the flapped airfoil was represented by a unit circle. Potential flow singularities such as sources, sinks, and doublets were added to the flow in the final transform plane to replicate the separation bubble created beneath the flap. Different arrangements of these singularities resulted in four different variations of the theoretical model. The model calculates the velocity and pressure distributions about the airfoil in the final transform plane, and then relays the information back to the original airfoil plane.

As mentioned, the experimental investigations were conducted on two different airfoils, the NACA 0018 airfoil, and the FXL III 142 airfoil. Each clean airfoil model had a chord of 24 inches, spanned the 15 inch high test section, and was equipped with a removable 10% chord leading edge Kruger flap. The wind tunnel used had its side walls replaced with arrays of evenly spaced airfoil slats at zero incidence. The airfoil slatted walls resulted in a test section that needed little or no boundary corrections. Each airfoil was equipped with a row of pressure taps located at mid-span which allowed the local static pressure to be measured at various points along the chord.

Agreement between experimental and theoretical results was poor at low angles of attack for all model variations, but became increasingly good as angle of attack increased, and as the influence of the separation bubble decreased. The model's accuracy reached a maximum in mid-range of angles of attack, from about $8°$ to $14°$. In this range, the agreement along the suction side

of the airfoils was excellent, and the agreement along the pressure side and bubble region was good for all four of the different models. As the angle of attack was increased to values near stall, non-linear and viscous effects became larger, and the models' accuracy decreased again.

Methods of increasing the accuracy of the models were tried. Mapping an airfoil artificially augmented by the displacement thickness of a turbulent boundary layer was found to bring the experimental and theoretical results into almost perfect agreement along the suction surface of airfoils at mid-range angles of attack. Averaging the theoretical results for slightly different mapping functions was also found to remove some of the oscillations in the theoretical pressure distributions near the leading edge.

Although there were some problems at both the low and high angles of attack, the potential flow model successfully predicted the pressure distributions along airfoils equipped with upper surface Kruger flaps in the middle range of angles of attack, where the flaps are most likely to be deployed.

Table of Contents

List of Figures

List of Variables

$A_j + iB_j$	jth Theodorsen coefficients
C	Chord of airfoil
C_l	Lift coefficient
C_p	Pressure coefficient
f	Mapping function
$F = \Phi + i\Psi$	Complex fluid potential
i	Square root of -1
k	Constant of proportionality representing the ratio of measured to published lift curve slope for the clean airfoil
m	Lift curve slope
n	Number of points defined along the airfoil profile for the Theodorsen transformation
p	Pressure
q, q_1, q_2	Source, sink, or doublet strength
r_0	Radial location of doublet
$\overline{R}$	Circle radius in Z_4 plane
R_3	Circle radius in Z_3 plane
$\mathrm{Re} = \frac{UC}{\nu}$	Reynolds number based on chord
u	First component of velocity
U	Free stream velocity
U_1	Local inviscid velocity
v	Second component of velocity
V	Free stream velocity in final transform plane
$w = u - iv$	Complex velocity
x	First coordinate in the complex physical plane

y	Second coordinate in the complex physical plane
$Z = x + iy$	Complex variable representing a point in physical plane
Z_{10}	Centroid of near circle in Z_1 plane
Z_j	Complex variable representing a point in an intermediate mapping plane

Greek characters

α	Angle of attack in physical plane
α_0	Angle of attack in final plane or rotation for final mapping
Γ	Vortex strength
$\delta, \delta_1, \delta_2$	Angular location of flow singularities in final plane
η	Second coordinate in the final transform plane
ν	Dynamic viscosity of fluid
ϕ_1, ϕ_2	Angular locations of separation and reattachment in Z_2 plane
Φ	Flow potential
$\overline{\phi}$	Angular mapping parameter in Z_3 and Z_4 planes
Ψ	Stream function
ρ	Fluid density
ξ	First coordinate in the final transform plane
$\zeta = \xi + i\eta$	Complex variable representing a point in the final transform plane

Subscripts

d	From the doublet model
m	Measured value, normally refering to the value at the entrance to the wind tunnel test section
max	Maximum value

p	Published value
R	Reattachment point
rd	From the radial doublet model
ret	Value at reattachment
S	Separation point
sep	Value at separation
ss	From the source and sink model
t	Corrected experimental value
TE	Value at the trailing edge
0	Stagnation value
2d	From the two doublet model
∞	Infinity

Acknowledgement

I would like to thank Dr. Parkinson for his advice and encouragement. His wealth of experience kept me learning constantly thoughout my stay here.

Also, I'd like to thank Sidney Chan, Matthew Findlay, Dragos Licu, and Mike Savage for always being there with a helping hand when it was needed. It was so much easier having advice, as well as a pool of able bodied workers, close by.

Chapter 1

Introduction

1.1 Typical Approaches to the Problem of Separated Fluid Flow

Low speed, separated flow arises in many different applications including wind-building inter-
actions, ocean currents around underwater obstructions, and even small aircraft wings during
take-off and landing. Engineers have been struggling with this problem for the latter half of
this century. Unfortunately, the flows involved are not yet completely understood, and this
complicates the solutions.

Typically, the problem is dealt with either through a computational or an analytical solution.
Neither solution method is exact. Turbulence, and the resulting Reynolds stresses, create
problems which are not directly solvable at the moment due to a superfluity of unknowns.
All of the computational methods in use model turbulence and its effects by creating extra
equations linking the properties of turbulence, while the analytical models try to ignore the
portions of the flow where turbulence controls the fluid properties. The only solution method
to deal with turbulence in a completely accurate manner is direct numerical simulation, and it
is incredibly time consuming to use, even for the simplest flows.

With the recent increase in both speed and storage capacities in computers, the computational
solutions have been gaining favour. This group of solutions involves splitting a typically external
flow into two different components. The first component comprises the main body of the flow
and is dealt with as a low turbulence flow where viscous effects are small. The second part of
the flow includes the separated region and the bounding shear layers, and is the region in which
viscous forces play a large role. Each region is solved in turn and the results are iterated until

the solution along the common interface converges. Such solutions are still computationally intensive, and involve modeling the turbulence in an empirically acceptable manner.

Analytical solutions, on the other hand, normally ignore turbulence, and thus the separated region, entirely. Using the geometry of the flow, in combination with the fluid properties, this group of solutions makes an educated guess at the location of the boundary between the two regions described above. The main body of the flow is then treated as an inviscid fluid, and the flow properties are determined. In order for this approach to be successful, the interface between the separated region and the main flow must be well defined and steady, so that the only effect of the separated region is to create a new boundary for the inviscid flow. In the case of a body immersed in the flow, the pressure of the fluid upon the body in the separated region must be approximated in another fashion. This group of solutions has the advantage of being simpler to implement and faster to solve than the computational methods, but it doesn't provide as complete a picture of the flow.

While the analytical models of separated flow aren't perfect, they can give valuable results. Direct testing of models in a wind tunnel environment is both time consuming and expensive. As mentioned above, numeric simulation of viscosity is also costly, and in the preliminary stages of design, possibly unnecessary. Here, an analytical model would be capable of giving a fast idea of the flow and an estimate of the resulting fluid forces. This allows alterations to the design to be made quickly and easily. Additionally, later on in the design process the results from an analytical model could be used as the input into a computational model, accelerating convergence time and reducing costs.

1.2 Previous Research in the Area

Modern research into analytical solutions to separated flow problems began in the mid 1950's with the work of Roshko and Woods.

In 1954, Roshko [13] published a hodograph theory extending the method of Helmholtz-Kirchhoff

for separated flow past a flat plate normal to the stream. In the original method, the wake was bounded by separation streamlines extending from the separation points at the tips of the plate. These streamlines simulated the free shear layers that exist in the real situation. Separation velocity and pressure were fixed at free stream values, an obviously unrealistic situation as it is well known that the pressure on the body in the wake region is lower than the free stream pressure. This produces faulty results for derived quantities, especially the drag on the body. Roshko modified the theory to permit the velocity at the separation point and thus the base pressure to vary, by providing the model with one empirical input, the velocity of the flow at the separation point. By increasing the velocity at separation, the base pressure is lowered. The theory was also altered to deal with symmetric (with respect to the free stream velocity) bluff bodies of arbitrary shape, resulting in a theory with many more real world applications.

The velocity along the separation streamlines in this model is constant until a finite distance downstream from the body, where it begins an asymptotic approach to the free stream value, adding a notch in the hodograph plane. Other hodographs allow the separation streamline velocity to vary in other ways from the separation point to infinity, but seemingly more realistic models (such as a continuous asymptotic decay towards the free stream value) do not yield results that are as accurate. This is an interesting little bit of empiricism in Roshko's otherwise well argued theory, but it is typical of solutions involving mathematical mappings that there are a bevy of mappings that accomplish the end goal, and that each mapping gives a slightly different result.

In 1955, Woods [17] extended the classical Helmholtz theory of incompressible flow about a flat plate in several ways, applying it to a circular cylinder in compressible subsonic flow, and a varying bubble pressure. Woods, like Roshko, saw that classical theory at the time made several quite invalid assumptions or had invalid results. For example, the current model in use was based on the work of Levi-Civita (developed around 1907, and extended in the 1920's), and it predicted wake widths that grew with downstream distance, so that the wake became infinitely wide. Additionally, except for Roshko's approach, the models available at the time required a wake of constant pressure. At infinity, the pressure in the wake must equal the free stream pressure. This meant that the pressure anywhere in the wake was equal to the free stream

pressure. Unfortunately, all physical wakes have a lower than free stream pressure behind the body, meaning that none of the models corresponded to reality. The errors in the formulation of these models also led to errors in the various results obtained.

Woods' method corrected these problems. He permitted a varying velocity distribution on the separation streamlines. The model assumes that the correct formulation would be the simplest one possible that yielded asymptotically parallel separation streamlines with a finite wake width at infinity. The theory only requires one experimentally known value, the pressure coefficient on the portion of the object covered by the wake. However, this method gives multiple values of the separation points for a given back pressure, and determining which result to use requires a knowledge of the actual separation points in the flow. This means that there are essentially two empirically determined variables needed.

The math involved is very long, complex, and more than a little tedious. Additionally, although the model deals with non-symmetric bluff bodies, it is still restricted to flows producing an infinite wake.

The next link in the chain of progress was both a step forward, and a slight step backwards. In 1970, Parkinson and Jandali [11] introduced their wake source model for bluff body potential flow. This theory used conformal mapping to reduce the problem of a symmetrical bluff body in an exterior flow to the well known problem of a circle in uniform flow. By adding ideal flow sources, an infinite wake of finite width is created. Like the previous two methods, this model requires the input of an empirically determined pressure coefficient at separation. Unlike the previous two models, it doesn't try to determine the separation points by flow properties, but instead allows them to be used as input into the model.

This approach was mathematically simpler than any of the models before it, and produced results that were as least as accurate, but it wasn't as flexible as Woods' model, as it couldn't deal with either non-symmetrical bodies or compressible flow.

As often happens in research, backing up out of a dead end and taking a slightly different approach opened up new avenues for dealing with more complex problems. In 1985, Parkinson

and Yeung [12] modified the theory and introduced the wake source model for airfoils with separated flow. By introducing new mapping techniques, and adding a vortex in the final transform plane to deal with the lifting effects of a non-symmetrical body, they managed to accurately model any airfoil shape with an upper surface spoiler or lower surface split flap. The empiricism involved was kept to a minimum, requiring only the pressure coefficient at separation, as well as the locations of separation, which are determined solely by the geometry of the airfoil and spoiler or flap.

Next, Yeung and Parkinson again modified the model to deal with one and two element airfoils experiencing trailing-edge stall, separation bubbles on flat plates, separation bubbles upstream of spoilers, and spoiler/slotted flap combinations, showing the versatility of the original approach. Now the model could not only deal with lifting bodies, but also with non-infinite separated flow regions.

Finally, in 1993, Brun [1] improved the theory to deal with a flat plate normal to the flow and separation bubbles on an airfoil by increasing the number of boundary conditions applied. Using this knowledge, Brun then modified the theory to deal with the case of an airfoil equipped with a Kruger flap, creating a lower surface separation region.

Unfortunately, there wasn't very much published data available on the pressure distributions along airfoils equipped with Kruger flaps. One of the few papers published on the subject, by Kruger himself in 1947 [6], had sketchy pressure data on a modified Mustang profile wing (subject to three-dimensional effects), and thus it was hard to determine how accurately the model was working.

This last work by Brun provides the impetus for the present study.

1.3 Direction of Current Research

The present study continues the work done by Sarah Brun. Specifically, it will provide data on the pressure distribution along two different airfoil profiles. This data will then be compared

with the predictions of the model, and the results from each profile contrasted. From these results, both the most effective configuration and the overall effectiveness of the model can be determined.

Chapter 2

The Potential Flow Model for Airfoils with Upper Surface Kruger Flaps

2.1 Introduction

As mentioned, Sarah Brun applied the ideas of Parkinson, Jandali, and Yeung to the problem of an airfoil equipped with an upper surface Kruger flap.

From the mid 1940's to the early 1950's, W. Kruger developed and tested a simple leading edge flap that could either be extended from the upper surface of an airfoil or rotated forward from the lower surface. Both of these arrangements are shown in figure 2.1. The flow about the lower surface flap is complicated, containing two separated regions, and so this research concentrates on the upper surface Kruger flap.

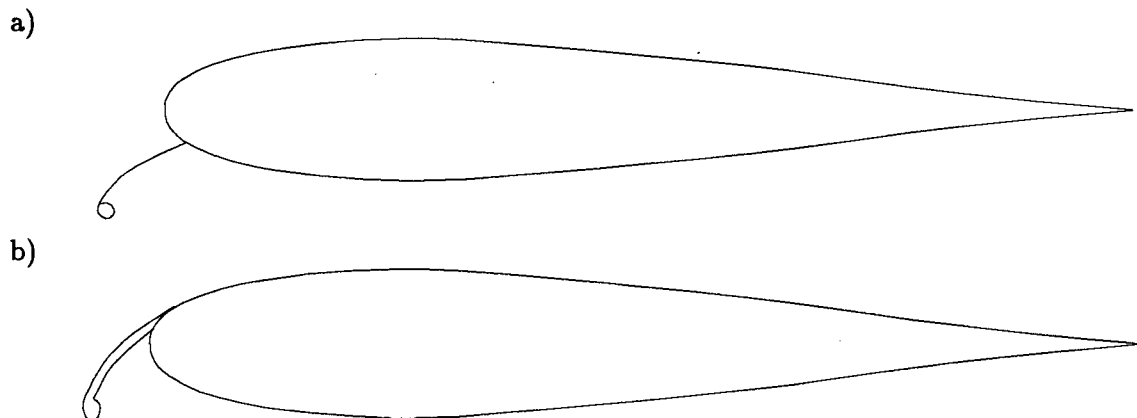Figure 2.1: Sketch of two different Kruger flap: a) Lower surface Kruger flap, b) Upper surface Kruger flap.

Both versions of this flap delay stall of the wing and increase C_{lmax} at the expense of an increase in C_d, making them useful during both take-off and landing of an aircraft. Additionally, when stall does occur, it is normally a trailing edge stall, and thus gentler. Other, more complex,

leading edge flap arrangements, like the multiple slat and flap systems in use on most passenger jets, may be more effective, but are more difficult and expensive to manufacture. On smaller planes, the Kruger flap represents a viable alternative, but even larger aircraft like the Airbus Super Transporter, the A310, and the Boeing 737 and 747 have made use of this flap.

The use of this flap by smaller aircraft is also an advantage for the aerodynamicist who wishes to model and test the flap in a university setting. Small, inexpensive aircraft tend to travel slowly, well below the speed of sound, where compressibility effects are negligible. This provides a two-fold benefit to the researcher. Firstly, few university wind tunnels are capable of testing in the transonic, supersonic, or even the high subsonic, range, but the results from a Kruger flap equipped airfoil tested in a low speed tunnel are still applicable. Secondly, the absence of compressibility effects means that incompressible theory can be used to create a simpler theoretical model.

2.2 Modeling the Flow

The streamlines about an unstalled airfoil equipped with a Kruger flap are sketched in figure 2.2. The flow separates from a point near the tip of the flap, and reattaches itself at a point further downstream on the lower surface of the airfoil, forming a separation bubble. The flow remains attached along the upper surface until stall.
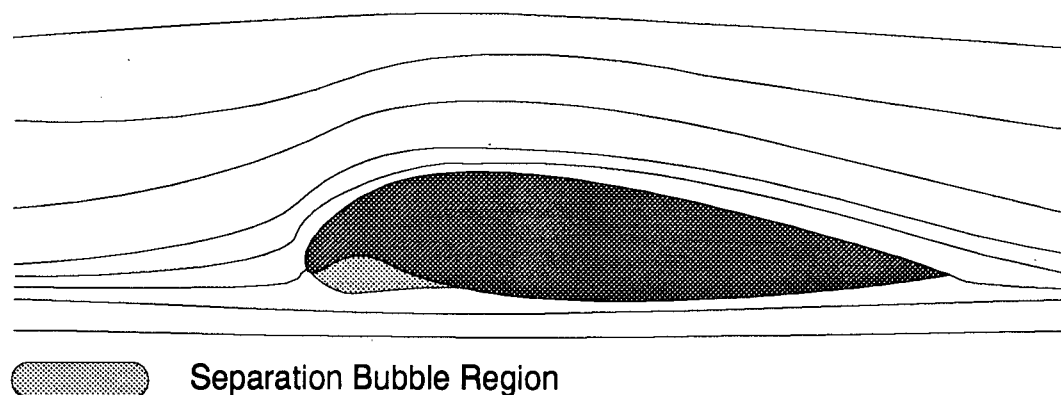

Separation Bubble Region

Figure 2.2: Streamlines about an airfoil equipped with a Kruger flap.

The model used is a potential formulation, which has several assumptions, requiring that the

flow remain two dimensional, incompressible, inviscid, and steady. Fortunately, the Kruger flap problem satisfies these assumptions fairly well.

Flow along a wing section of reasonably large aspect ratio remains approximately two dimensional except near the tips. As already mentioned, most Kruger flap applications are at low speeds, and so the flow can be well approximated as incompressible. Additionally, the flow around the airfoil is essentially inviscid, except in the boundary layers and inside the separation bubble. The boundary layers are usually small and have a negligible effect on the pressure distribution and lift at these speeds. The effects of viscosity in the separation bubble are not negligible, meaning that the model is not capable of calculating details of the flow within the separation bubble. However, the boundaries of the separation bubble are assumed to be well defined and steady, meaning that fluid properties just outside of the separation bubble can be determined. Finally, only steady flow is dealt with. This doesn't mean that the flow within the separation bubble itself is steady, but instead that the shear layer representing the boundary of the bubble is steady.

2.3 Brun's Conformal Mapping Solution

Solid bodies in fluid dynamics are represented by requiring that there must be no flow through the exterior of the body. In complex potential flow, there is no flow across streamlines, and therefore the body is represented by a streamline of the same shape as the body. Once this streamline is found, the fluid properties along it can be determined, and the forces on the body calculated.

Complex potential flow theory defines the fluid potential as:

$$F(\zeta) = \Phi + i\Psi \qquad (2.1)$$

and the complex velocity as the first derivative of the complex potential:

$$w(Z) = \frac{dF(Z)}{dZ} = u - iv \tag{2.2}$$

where $Z = x + iy$ is a complex variable representing location in a plane.

As the flow was assumed to be two dimensional, incompressible, and inviscid, the Bernoulli equation can be applied to determine the pressure coefficient:

$$\frac{p}{\rho} + \frac{w(Z)^2}{2} = \frac{p_\infty}{\rho} + \frac{U^2}{2}$$
$$C_p = \frac{p - p_\infty}{\frac{1}{2}\rho U^2} \tag{2.3}$$

where p is the local static pressure, ρ is the fluid density, and p_∞ and U respectively represent the free stream pressure and velocity.

The pressure coefficient can then be used to determine the forces on the body, if required.

It's difficult, however, to find and deal with streamlines that accurately represent arbitrary shapes. It would be ideal if only one simple body had to be modeled, and the results from that body could be applied to other shapes. A good candidate for the simple shape would be the circle, which has been studied extensively, and can be easily modeled in potential flow theory by the doublet, with a vortex at the origin to simulate the lifting properties of the airfoil. Happily, there is a way of doing exactly this.

Conformal mapping is a powerful branch of mathematics that uses analytical functions to stretch and mold space so that shapes inscribed thereupon can be transformed into other shapes. Each point in one plane, defined previously as $Z = x + iy$, is mapped to another plane, for example $\zeta = \xi + i\eta$, by the transform function:

$$Z = f(\zeta) \tag{2.4}$$

By choosing the correct series of mappings, it is possible to map most closed shapes, including almost any airfoil, to a plane in which they are represented by the familiar circle. Additionally, the Milne-Thomson circle theorem provides an avenue to add other flow elements, such as sources, sinks, or vortices, to the flow without disturbing the original circular streamline, allowing the simulation of more complicated flows.

Conformal mapping using analytical functions also has a key property: angles of intersection of curves are preserved in both magnitude and sense. If two line segments meet in the original plane at an angle of δ, they will meet at the same angle δ in the transform plane. As with any rule, there is always an exception. At critical points of the mapping function (where the first derivative of the mapping function has a zero), the angles of intersection are preserved in sense but increased in magnitude by a factor equal to one greater than the order of the zero, i.e. first order zeroes double the angle of intersection, second order zeroes triple it, etc.

Of course, being able to transform an airfoil into a circle, and solve the flow about the circle, is only useful if there exists a method of translating the information back into the original airfoil plane. Indeed, given the velocity in the final transform plane and the first derivative of the mapping function, it is not difficult to find the velocity in the initial plane. As defined in 2.2:

$$
\begin{aligned}
w(Z) = \frac{dF}{dZ} &= \frac{dF}{d\zeta}\frac{d\zeta}{dZ} \\
&= \frac{dF/d\zeta}{dZ/d\zeta} \\
&= \frac{w(\zeta)}{f'(\zeta)}
\end{aligned}
\tag{2.5}
$$

The models used have the following properties:

i) Only the wetted surface of the airfoil is mapped. The section contained within the separation bubble is ignored, and the rest of the airfoil becomes an airfoil slit. The separation and reattachment points, as well as the trailing edge, are made simple zeroes of the complete mapping function, so that angles there are doubled. At separation and reattachment, the corresponding

lines on the circle meet at 180° in the final transform plane, meaning that they meet at 360° in the physical plane, and are thus cusps, as expected in an airfoil slit. The separation and reattachment streamlines, which intersect the body at 90° in the final mapping plane are tangential to the body in the original plane. The trailing edge also becomes a cusp or wedge in the physical plane.

ii) As mentioned, the portion of the airfoil within the separation bubble is ignored. The bubble is assumed to have relatively small normal shear forces, meaning that the normal pressure gradient is small. Therefore, the pressure along the streamline representing the separation bubble is assumed to be equivalent to the pressure exerted on the airfoil at that position along the chord, as shown in figure 2.3.
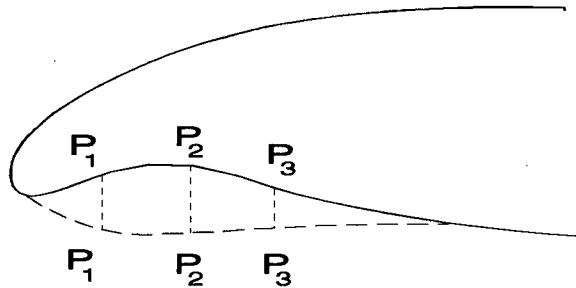
Figure 2.3: Pressure on the bubble is equivalent to pressure on the airfoil at that position along the chord.

iii) The shear layer forming the separation bubble is assumed to be thin, well defined, and steady. It is represented by a separation streamline extending from the separation point to the reattachment point. The separation and reattachment points are considered known and used as inputs to all of the models.

iv) All of the flow calculations are performed in the final transform plane, where, as already mentioned, the airfoil is represented by a circle, and the computations are much simpler. Once all of the relevant quantities have been determined, they are relayed back to the original physical plane.

2.4 The Mapping

Mapping an arbitrary airfoil into a circle is not a one step process. Several consecutive mappings are needed, and the mappings used will now be described.

The beginning physical plane contains the airfoil and Kruger flap to be mapped. Both the original airfoil and the flap are treated as a single airfoil. The trailing edge of the airfoil is located at +2 on the x-axis, and the point half way between the leading edge of the airfoil and the center of curvature of the leading edge is placed at -2. The mapping sequence is illustrated in figure 2.4.

The first step is to apply a Joukowsky transformation.

$$Z = Z_1 + \frac{1}{Z_1} \tag{2.6}$$

This transforms a Joukowsky airfoil into a perfect circle. Most airfoils have shapes similar to the Joukowsky airfoil, and so the airfoil is mapped to a shape that is almost a circle. Any real airfoil, with either thickness or camber, will form a near circle centered slightly off the origin. The first derivative of the Joukowsky transform has a simple zero at $Z_1 = 1$, which represents the trailing edge of a thick airfoil. Thus the trailing edge becomes a simple zero of the first deriviative of the complete transform function. $Z_1 = -1$ is also a simple zero of the first derivative of the mapping function, but represents a point in the interior of a thick airfoil, and therefore is of no consequence to the model.

The next mapping shifts the near circle by the distance from its centroid to the origin. This centers the near circle on the origin. Z_{10} is the distance from the centroid to the origin.

$$Z_1' = Z_1 - Z_{10} \tag{2.7}$$

Now, a Theodorsen transform, as described in references [1] and [15], iteratively maps the near

circle to a perfect circle by applying the following infinite series.

$$Z_1' = Z_2 \exp \left[\sum_{j=0}^{\infty} \frac{A_j + iB_j}{Z_2^j} \right] \tag{2.8}$$

Practically, this series is truncated by determining n points on the near circle that will be mapped to a perfect circle. As there are two coefficients for each j, these n points allow $n/2$ Theodorsen coefficients A_j and B_j to be determined.

$$Z_1' = Z_2 \exp \left[\sum_{j=0}^{n/2} \frac{A_j + iB_j}{Z_2^j} \right] \tag{2.9}$$

The airfoil has now been mapped to a perfect circle. As mentioned previously however, the model requires that both the separation and attachment points become simple zeroes of the complete mapping function, which has not been accomplished yet.

The portion of the airfoil between the separation and reattachment points is discarded, and the circle becomes a circular arc slit. The slit is rotated and scaled so that the newly formed cusps are located at $2i$ and $-2i$.

$$Z_2 = \left[\frac{Z_3}{R_3} + \cos(\frac{\phi_2 - \phi_1}{2}) \right] e^{i(\frac{\phi_1 + \phi_2}{2})} \tag{2.10}$$

where ϕ_1 and ϕ_2 are the angular locations of the separation and reattachment points in the Z_2 plane, and R_3 is the radius of the circle in the Z_3 plane.

A modified Joukowsky transform then opens this airfoil slit into a full circle which is simultaneously translated to the origin. This mapping creates the necessary simple zeroes in the mapping function at the separation and reattachment points, which are located at $\overline{R}cos\overline{\phi} + i$ and $\overline{R}cos\overline{\phi} - i$ in the plane of the full circle, where $\overline{R}$ is the radius of the circle in the Z_4 plane. From the geometry of the mapping, $4\overline{\phi} = \phi_2 - \phi_1$, and so $\overline{\phi} = \frac{\phi_2 - \phi_1}{4}$.

$$Z_3 = Z_4 - \cot\overline{\phi} - \frac{1}{Z_4 - \cot\overline{\phi}} \tag{2.11}$$

Finishing it all off, the circle is scaled and rotated to obtain a unit circle at zero incidence to the oncoming flow. This simplifies the mathematics in the final plane.

$$Z_4 = \overline{R}\zeta e^{i\alpha_0} \tag{2.12}$$

where α_0 is the incidence of the flow in the second last transform plane.

It is easily shown that:

$$\overline{R} = \frac{1}{\sin\overline{\phi}}; \text{ and}$$

$$R_3 = \frac{\overline{R}}{\cos\overline{\phi}}. \tag{2.13}$$

To find the velocity in the physical plane using equation 2.5, the first derivative of the complete mapping function must be known. Applying the chain rule yields: $\frac{dZ}{d\zeta} = \frac{dZ}{dZ_1}\frac{dZ_1}{dZ_2}\frac{dZ_2}{dZ_3}\frac{dZ_3}{dZ_4}\frac{dZ_4}{d\zeta}$. At most of the points along the airfoil, this is easily calculated, giving:

$$\frac{dZ}{d\zeta} = \cos\overline{\phi}\left[1 - \frac{1}{Z_1^2}\right]\left[1 + \frac{1}{(Z_4 - \cot\overline{\phi})^2}\right]e^{i(\alpha_0 + \frac{\phi_1 + \phi_2}{2})}\frac{dZ_1}{dZ_2}$$

where:

$$\frac{dZ_1}{dZ_2} = \left[1 - \sum_{j=0}^{n/2} j\frac{A_j + iB_j}{Z_2^j}\right]\exp\left[\sum_{j=0}^{n/2}\frac{A_j + iB_j}{Z_2^j}\right] \tag{2.14}$$

At an infinite distance from the origin, no disturbance from the airfoil should be seen, and the flow should be uniform and at the same incidence. Therefore, at $Z_1 = Z_2 = Z_4 = \infty$:

$$\frac{dZ}{d\zeta}\Big|_\infty = \cos\overline{\phi}e^{i(\alpha_0 + \frac{\phi_1 + \phi_2}{2})}e^{A_0 + iB_0} \tag{2.15}$$

giving:

$$V = U\cos\overline{\phi}e^{A_0}$$

$$\alpha_0 = \alpha - B_0 - \frac{\phi_1 + \phi_2}{2} \tag{2.16}$$

V is the magnitude of the incident velocity in the final plane.

Now, all of the variables in the mapping functions can be calculated.

Examining equation 2.14, it is noted that the points $Z_1 = 1$, the trailing edge, $Z_4 = cot\overline{\phi} - i$, the separation point, and $Z_4 = cot\overline{\phi} + i$, the reattachment point, are all critical points of the complete mapping function. From equation 2.5, these critical points create indeterminate velocities in the real plane, as both the numerator and the denominator approach zero. In order to evaluate the velocities at these points, it is necessary to apply L'Hopital's rule:

$$\lim_{\zeta \to \zeta_0} \frac{w(\zeta)}{f'(\zeta} = \frac{w'(\zeta)}{f''(\zeta)} \tag{2.17}$$

where:

$$f'' = \left| \frac{d^2 Z}{d\zeta^2} \right| = 2\cos^2\overline{\phi} \left| \left(1 + \frac{1}{(Z_4 - \cot\overline{\phi})^2} \right) \frac{dZ_1}{dZ_2} \right|^2 \tag{2.18}$$

at the trailing edge, and:

$$f'' = \left| \frac{d^2 Z}{d\zeta^2} \right| = 2\overline{R}\cos\overline{\phi} \left| \left(1 - \frac{1}{Z_2^2} \right) \frac{dZ_1}{dZ_2} \right| \tag{2.19}$$

at the separation and reattachment points.

Now, it is important to realize that the choice of mappings used is arbitrary. Other mapping sequences that create critical points at the necessary locations, and result in a unit circle in the final transform plane, are just as valid as the sequence used here. Choosing other mappings may result in slightly different pressure distributions in the separation bubble region.

2.5 Flow Models

All of the flow models model the physical airfoil by a doublet forming a unit circle, located at the origin of the final transform plane. A uniform flow is then added, simulating the motion of the airfoil through the air. The circulation about the airfoil is modeled by a vortex, also at the origin of the final transform plane. Brun developed two models that introduce either one or two doublets located on the unit circle. Two new models have since been added which involve adding either a source/sink combination on the unit circle, or a single doublet not located on

the circle. Each of the four variations uses the flow singularities, all located in the region of separation, to create a separation streamline from the separation point to the reattachment point.

There are three boundary conditions that are intrinsic to all of the models. To avoid infinite pressure coefficients, all three of the critical points of the mapping function must be also stagnation points in the final plane.

2.5.1   Single Doublet

The simplest model adds a doublet to the flow, located on the unit circle at an angle δ somewhere in the region of separation. Milne-Thomson's circle theorem is used to calculate the strength and position of the image doublet within the unit circle. This situation is described in reference [1]. From potential flow theory, the potential is given by:

$$F(\zeta) = V(\zeta + \frac{1}{\zeta}) + i\Gamma \log \zeta - iq\frac{e^{i\delta}}{\zeta - e^{i\delta}} \tag{2.20}$$

and the velocity:

$$w(\zeta) = V(1 - \frac{1}{\zeta^2}) + i\frac{\Gamma}{\zeta} + i\frac{qe^{i\delta}}{(\zeta - e^{i\delta})^2} \tag{2.21}$$

This results in three unknowns, q, the strength of the doublet, δ, the angular location of the doublet, and Γ, the circulation about the airfoil. The three boundary conditions then provide a closed problem, and the unknowns can be determined. The solution method is well described in reference [1], hereafter referred to as Brun.

2.5.2   Source and Sink

An alternative is to add a source and sink of equal strength, q, at angles δ_1 and δ_2 along the body streamline. This introduces an additional unknown, requiring an extra boundary condition. The largest discrepancy between the predictions of the single doublet and experimental results occurs at the separation point, and so it seems logical to choose the pressure coefficient at this

point as the next boundary condition. With four unknowns, and four boundary conditions, the problem is again closed. The potential, velocity, and velocity gradient in the final plane are:

$$F(\zeta) = V(\zeta + \frac{1}{\zeta}) + i\Gamma \log \zeta + q \left[\log(\zeta - e^{i\delta_1}) - \log(\zeta - e^{i\delta_2}) \right] \tag{2.22}$$

$$w(\zeta) = V(1 - \frac{1}{\zeta^2}) + i\frac{\Gamma}{\zeta} + q \left[\frac{1}{\zeta - e^{i\delta_1}} - \frac{1}{\zeta - e^{i\delta_2}} \right] \tag{2.23}$$

$$w'(\zeta) = \frac{2V}{\zeta^3} - i\frac{\Gamma}{\zeta^2} + q \left[\frac{1}{(\zeta - e^{i\delta_2})^2} - \frac{1}{(\zeta - e^{i\delta_1})^2} \right] \tag{2.24}$$

At the critical points, after some manipulation the boundary conditions become:

$$w(\theta_{sep}, \theta_{ret}, \theta_{TE}) = 0 = 2V \sin \theta + \Gamma + \frac{q}{2} \left[\cot \left(\frac{\theta - \delta_2}{2} \right) - \cot \left(\frac{\theta - \delta_1}{2} \right) \right] \tag{2.25}$$

and

$$C_{p\,sep} = 1 - \left(\frac{w'(\zeta)}{f''(\zeta)} \right)^2 \tag{2.26}$$

The most robust solution method found was to iteratively satisfy the boundary conditions as follows.

i) Set δ_1 so that $w(\theta_{sep}) = 0$;

ii) Set δ_2 so that $w(\theta_{ret}) = 0$;

iii) Set q so that

$$\frac{w'(\zeta_{sep})}{f''(\zeta_{sep})} = \sqrt{1 - C_{p\,sep}}; \text{ and}$$

iv) Set Γ so that $w(\theta_{TE}) = 0$.

Repeat from step i) until error is sufficiently small.

It seems probable that the source and sink are approximately evenly spaced between the separation and reattachment points, and so initial guesses of $\delta_1 = \theta_{sep} + (\theta_{ret} - \theta_{sep})/3$, and $\delta_2 = \theta_{sep} + 2(\theta_{ret} - \theta_{sep})/3$ are used. At the trailing edge, the contribution of the source and sink should be small, so an initial guess of $\Gamma = -2V \sin \theta_{TE}$ seems proper. Finally, the initial strength of the source and sink is set arbitrarily to a value of 0.

2.5.3   Radial Doublet

Both the single doublet and the source and sink models result in fairly thin separation bubbles at low angles of attack. This is at least partly a property of the mappings used. Examining the mapping, it seemed that a thicker bubble might result if the circular bubble in the final transform plane were shifted radially either a little outwards or a little inwards. The one doublet model was modified to allow the doublet to be placed at a radius r_0 in the final transform plane, instead of directly on the body streamline as was the case previously. This introduced another unknown into the model, and again the separation pressure coefficient was used to close the model. The mathematics for this situation become more complicated, but are still easily solved. The potential, velocity, and velocity gradient created by the radial doublet alone are given by:

$$F_{rd} = q\frac{\zeta r_0 - e^{i\delta} - \zeta^2 e^{i\delta} + \zeta r_0 e^{i2\delta}}{(\zeta - r_0 e^{i\delta})(\zeta r_0 - e^{i\delta})} \tag{2.27}$$

$$w_{rd} = -q\frac{\zeta^2 r_0^2 - \zeta^2 e^{i2\delta} + 2\zeta r_0 e^{i3\delta} - r_0^2 e^{i4\delta} - 2\zeta r_0 e^{i\delta}}{(-\zeta + r_0 e^{i\delta})^2(\zeta r_0 - e^{i\delta})^2} \tag{2.28}$$

$$w'_{rd} = -2q\frac{3\zeta r_0 e^{i2\delta} - \zeta^2 r_0^2 e^{i\delta} - 3\zeta r_0^3 e^{i4\delta} - \zeta^3 r_0 e^{i2\delta} + 3\zeta^2 r_0^2 e^{i3\delta} + \zeta^3 r_0^3 + r_0^4 e^{i5\delta} - e^{i3\delta}}{(-\zeta + r_0 e^{i\delta})^3(\zeta r_0 - e^{i\delta})^3} \tag{2.29}$$

These values are then added on to the potential, velocity, and velocity gradient created by the origin centered doublet, the lifting vortex, and the uniform incident flow.

As in the source and sink model, an iterative method is used to determine the values of the unknowns. It is assumed that r_0 will be fairly close to one, and therefore that the values for δ, q, and Γ from the original single doublet model are used as initial guesses. From there, the following boundary conditions are applied iteratively:

i) Set Γ so that the trailing edge is a stagnation point;

ii) Set q so that the separation point is stagnated;

iii) Set δ so that the reattachment point is stagnated; and

iv) Set r_0 so that the pressure coefficient at separation is the desired value.

Repeat from step i) until the error has been reduced to an acceptable value.

2.5.4 Two Doublets

Brun's other variation on the model was to introduce two doublets, of strengths q_1 and q_2, at angles δ_1 and δ_2, in the region of separated flow on the body streamline. With 5 unknowns, two extra boundary conditions are needed. The pressure coefficients at both the separation and reattachment positions seem the most logical values to use. This allows a little more control over the pressure distribution along the separation bubble, but also adds an extra degree of empiricism. The resulting potential and velocity are given as:

$$F(\zeta) = V(\zeta + \frac{1}{\zeta}) + i\Gamma \log \zeta - iq_1 \frac{e^{i\delta_1}}{\zeta - e^{i\delta_1}} - iq_2 \frac{e^{i\delta_2}}{\zeta - e^{i\delta_2}} \tag{2.30}$$

$$w(\zeta) = V(1 - \frac{1}{\zeta^2}) + i\frac{\Gamma}{\zeta} + i\frac{q_1 e^{i\delta_1}}{(\zeta - e^{i\delta_1})^2} + i\frac{q_2 e^{i\delta_2}}{(\zeta - e^{i\delta_2})^2} \tag{2.31}$$
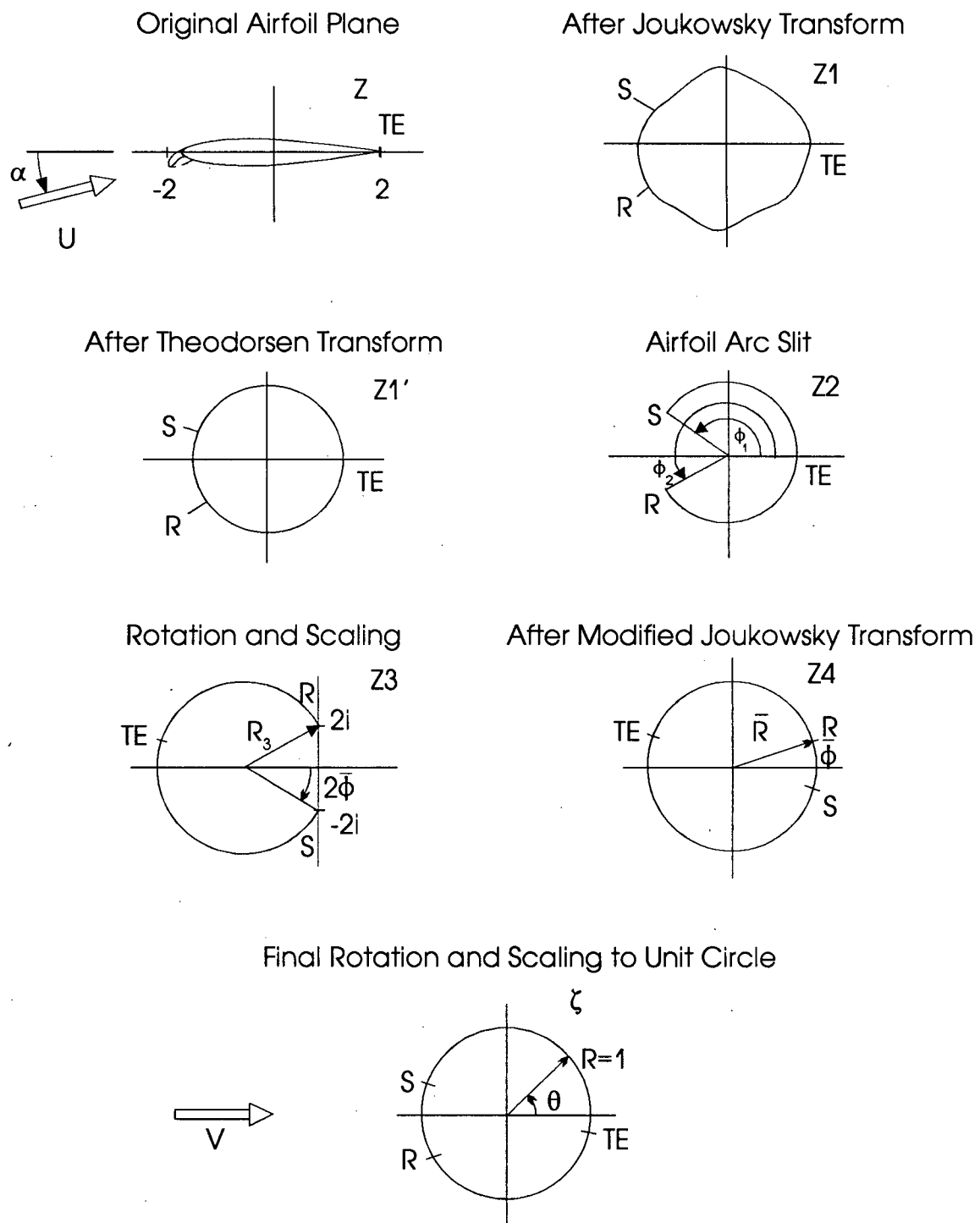
Again, the solution method is well described in Brun.

Figure 2.4: The mapping sequence.

Chapter 3

Experimental Conditions

3.1 The Wind Tunnel

All experiments were performed in UBC's Green wind tunnel, a recirculating tunnel with an 8.5' long test section. The Green tunnel was equipped with two dimensional test section (2DTS) inserts, further described in references [3],[10], and [16], which alleviate the effects of blockage, curvature, and downwash that occur in most wind tunnel testing, removing the need to apply boundary corrections to the experimental data. These inserts altered the test section by replacing the solid side walls with airfoil slatted walls with an open air ratio of 0.60. The test section had a height of 15" and a width of 36".

The entrance to the test section in the Green wind tunnel is equipped with a ring of four connected pressure taps. These taps allow the static pressure at the test section entrance to be measured. All initial airfoil pressure tap measurements are made relative to this static pressure. An additional pressure tap in the upstream settling chamber allows the stagnation pressure to be determined. From the static and stagnation pressure, the velocity at the test section entrance can be calculated.

$$U_m = \left[\frac{2(p_0 - p_m)}{\rho} \right]^{1/2} \tag{3.1}$$

The airfoils are mounted on a six component force balance, which can measure lift, drag, side force, roll, pitch, and yaw. For this research, only lift and drag measurements were made, and only lift measurements were used.

3.2 The Airfoils

Two separate airfoil profiles were tested to provide a comparison of both the effects of the flap and the predictions of the models for different airfoil shapes. Both Kruger flaps were designed to be removable, so that the clean airfoils could be tested. Each clean airfoil had a 24" chord and spanned the 15" high test section. The airfoils were equipped with a row of pressure taps along the midspan line on both the suction and pressure surfaces. The taps were placed about half an inch apart near the leading edge, and then about one inch apart until about two or three inches from the trailing edge, where the airfoils became too thin to tap.

The NACA 0018 airfoil, shown in figure 3.1, was chosen as an example of a thick, low Reynolds number airfoil. It reaches its maximum thickness of 18% at 30% chord. The clean airfoil is symmetrical.

The coordinates used for the mapping sequence of this airfoil can be found in appendix A. This airfoil has a large leading edge radius, and a fairly linear lift curve. It typically stalls at an angle of about 16 degrees. The model of the clean airfoil had 53 pressure taps, which was increased to 56 taps when the flap was added.
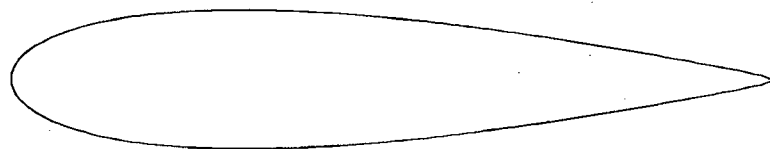
Figure 3.1: NACA 0018 profile.

The other airfoil selected was the FXL III 142, which also performs well at low Reynolds numbers. This airfoil is thinner, with a maximum thickness of 14.2% at 30% chord. It has a small leading edge radius, and a lift curve slope that remains very linear almost to stall, which occurs at about 12 degrees. This profile is sketched in figure 3.2. There were 48 pressure taps on the clean airfoil, and 53 taps once the flap was installed.

Both the clean airfoil coordinates and the coordinates for the mapping of the Kruger flap equipped airfoil can be found in appendix A. Coordinates for this airfoil, and the previously
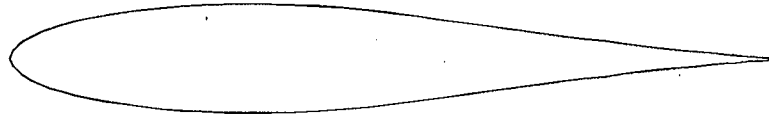
Figure 3.2: FXL III 142 profile.

published lift and drag data for both airfoils are taken from reference [8].

3.2.1 The Upper Surface Kruger Flap

The flap is designed to simulate a flap that retracts smoothly into the leading edge of the airfoil. Both flaps are 10% chord flaps, which is a typical size for this application. The profile for the first half of the flap is identical to the clean airfoil profile to the 5% chord position. The second half of the flap is a portion of a circular arc created by fitting an arc to three points on the original profile of the airfoil. One point is chosen at close to 2.0% chord, one point at 5.0% chord, and one point between the previous two. The flap would be extended on a real wing by rotating it forward through this arc. Because the arc forms a portion of the original profile, the flap fairs smoothly into the airfoil, attaching at the first point on the arc, at 2.0% chord. The small extension of the flap past the 10% chord point is necessary if the flap is to join the airfoil at this point. This is sketched in figure 3.3, adapted from reference [2].

In the construction of the models, the flap was made thick enough to allow pressure taps to be added along the mid span line, and to ensure that the flap would not easily break. The thickness of the flap on the model is not of large importance, as the underside of the flap is in the separated region, where small changes in shape do not greatly affect the flow. A problem arises when one attempts to map the exact profile for the models, as the Theodorsen mapping will not converge for airfoils with abrupt changes in curvature, such as the regions between the underside of the flap and the leading edge ball, and the edge of the flap and the underside of the original profile. As the region between separation and reattachment is discarded in the mappings to form the airfoil slit, it seems acceptable to exclude the small part of this region from just after the tip of the leading edge ball to a point along the original profile at about two or three percent chord. This allows the Theodorsen mapping to converge easily.
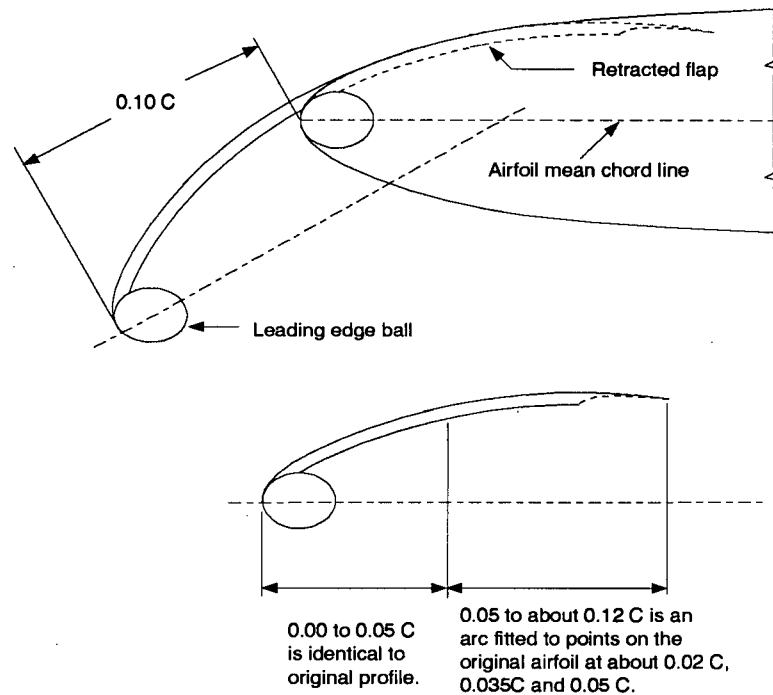
Figure 3.3: Flap construction.

3.3 Comparison Between Experimental Results and Published Data for Lift

Figure 3.4 shows a comparison between a published lift curve for the clean FXL III 142 airfoil, and the results of measurements from the 2DTS. The published lift curve has a slope, m, of about 0.1038, while the measured lift curve slope is lower at 0.0864. A careful examiner will note that the disagreement between experimental and published lift coefficients is not as large at negative angles of attack. This does not indicate a problem with the experimental lift curve, which has the same slope in both the positive and negative α quadrants, but instead it shows a slight asymmetry in the published data.

This disagreement between measured and previously published data is constant in all of the lift curves at various Reynolds numbers for both airfoils. Within experimental error, all of the measured data is low by a constant, $k = m_m/m_p = 0.842$. This is an indication of a problem somewhere within the experimental apparatus. Extensive testing failed to reveal the source of the low loadings, which were also seen in the pressure measurements. It was not due to the 2DTS airfoil slatted walls, as the loads were also low by the same constant when the airfoil

slats were replaced with solid walls, and conventional boundary corrections were applied to the data.

FXL III 142 in 2DTS
Uncorrected lift coefficient vs. angle of attack
Rec = 1.0 E 6

▲   Measured Lift Coefficient
□   Published Data

m published: 0.1038
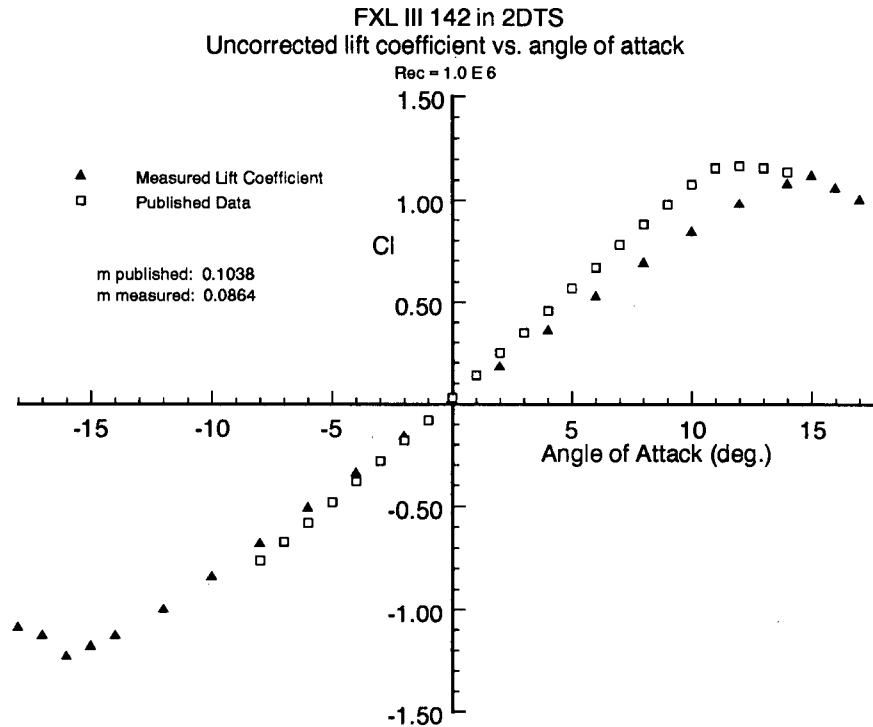m measured: 0.0864

Cl

Angle of Attack (deg.)

Figure 3.4: Discrepancy between measured and published lift curves.

For a valid comparison between the experimental pressure distributions and those of the theoretical models, the data must in some way be corrected to compensate for the disparity. There are two simple ways to correct for low loadings in wind tunnel testing.

The first assumes that all of the pressure and lift measurements are linearly low. To correct the lift curve and pressure measurements, define:

$$C_{lt} = C_{lm}\frac{m_p}{m_m} = C_{lm}\frac{1}{k}$$

$$C_{pt} = C_{pm}\frac{m_p}{m_m} = C_{pm}\frac{1}{k} \tag{3.2}$$

This approach obviously corrects the lift curve slope. Unfortunately, the uncorrected pressure data includes pressure coefficients very close to stagnation ($C_p = 1$) at points near the tip of the flap. Applying this correction means that the pressure coefficient at these points becomes

greater than one, which is not physically meaningful. This method is obviously not applicable.

The second method is commonly used in airfoil testing, and assumes that both the velocity and pressure have been correctly measured somewhere upstream, but that the velocity changes before reaching the test section. This seems to be the situation that applies in this case, as both total head and dynamic pressure are measured just upstream of the test section, and pressures near or at stagnation are being measured along the airfoil. If there are no (or negligible) losses in the flow, any change in the free stream velocity as the flow enters the test section will also result in a change in free stream pressure, p_∞. In these experiments, both the measurements of lift and pressure coefficients are low, and the only variable shared between the two equations is the free stream velocity, U. Therefore, the constant k can also be defined as:

$$k = \frac{U_t^2}{U_m^2} = \frac{m_m}{m_p} \qquad (3.3)$$

This change in free stream velocity also results in a change in free stream pressure of:

$$p_{\infty t} = p_{\infty m} + \frac{1}{2}\rho U_m^2 (1 - k) \qquad (3.4)$$

giving the following correction for the pressure coefficient:

$$C_{pt} = C_{pm}\frac{1}{k} - \frac{1-k}{k} \qquad (3.5)$$

or

$$1 - C_{pt} = (1 - C_{pm})\frac{1}{k} \qquad (3.6)$$

The corrections applied to the lift coefficient remain the same as in the first method.

This method preserves stagnation points, corrects the lift measurements, and provides good agreement for the pressure coefficient along the entire chord of the airfoil. It also seems to be

the method that most correctly simulates the experimental set up. It has been applied to all of the data that follows.

Chapter 4

Results and Discussion

4.1 Measured Lift Curves

4.1.1 Clean Airfoils

To insure that the clean airfoil models were symmetrical and behaving properly, their lift curves were measured over a range of angles of attack using the six component force balance, and the data was compared with published data from reference [8]. The results for both airfoils are shown below, in figures 4.1 and 4.2.
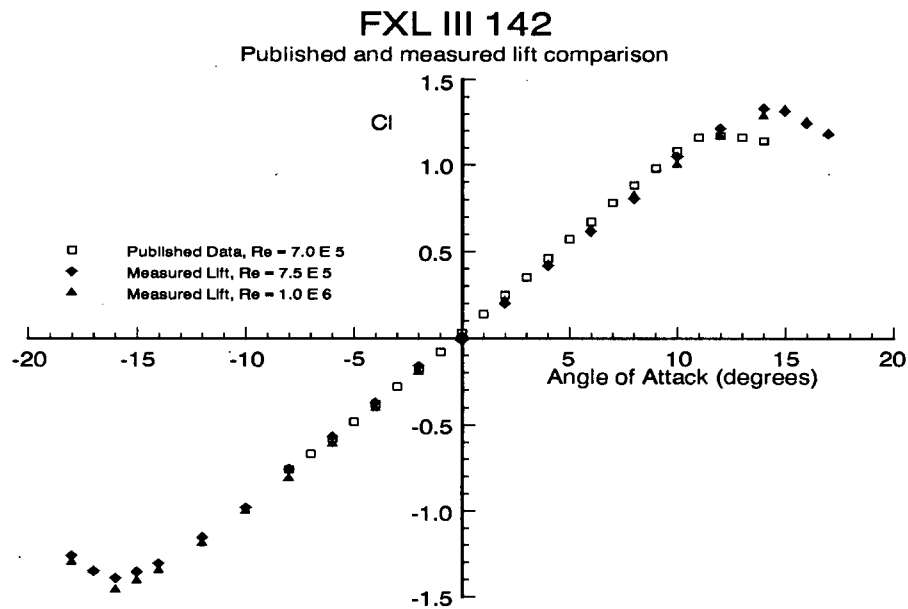
Figure 4.1: FXL III 142: published and experimental lift comparison.

The clean FXL airfoil results compared very well to the published data at both of the Reynolds numbers tested. The lift curve was almost completely symmetric about zero, and remained linear almost to the point of separation. The results were independent of Reynolds number to within experimental error. As mentioned in the previous chapter, agreement is better at negative angles of attack, which is a result of a slight lack of symmetry in the published data. Experimental stall occurs at 15° or 16°, as compared with about 12° in the published data. Stall for a low Reynolds number airfoil is typically boundary layer controlled, and the change in stall angle probably arises from different surface conditions on the tested airfoils, which could easily be the result of the manufacturing methods used. As lift and pressure distribution results for both Reynolds numbers tested were virtually identical, only the Re = 1.0 E 6 results will be used, saving needless repetition.
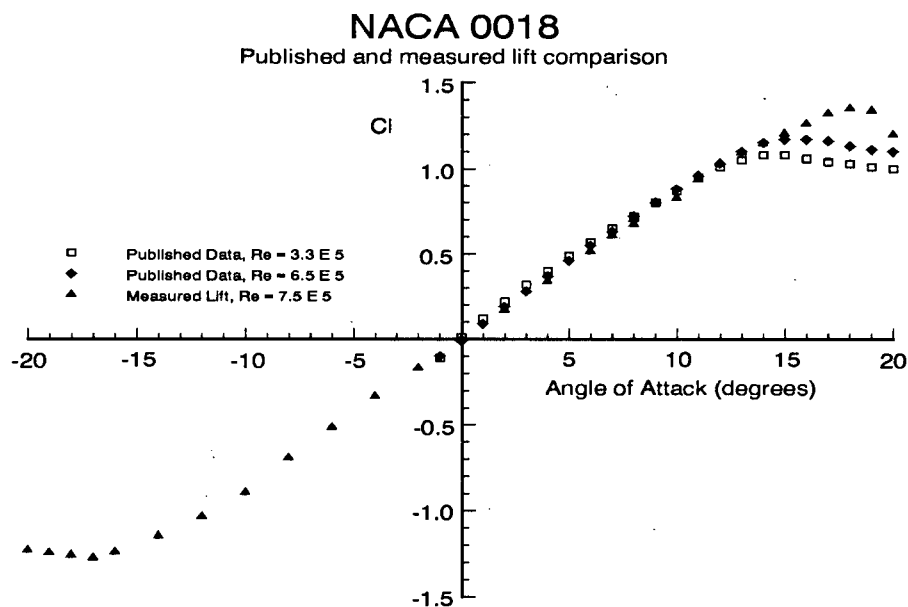
Figure 4.2: NACA 0018: published and experimental lift comparison.

Agreement for the NACA airfoil is also very good at low angles of attack. This airfoil is far more sensitive to boundary layer effects than the FXL airfoil in the range from Re = 1.0 E 5 to 1.5 E 6, which is also the range that can be tested in the Green wind tunnel. Published lift curve slopes range from 0.086 to 0.095, and stall angles vary from 12° to 16°, with 16° being by far the most prevalent. The lift curves chosen for comparison seemed to be the most reliable ones in this range.
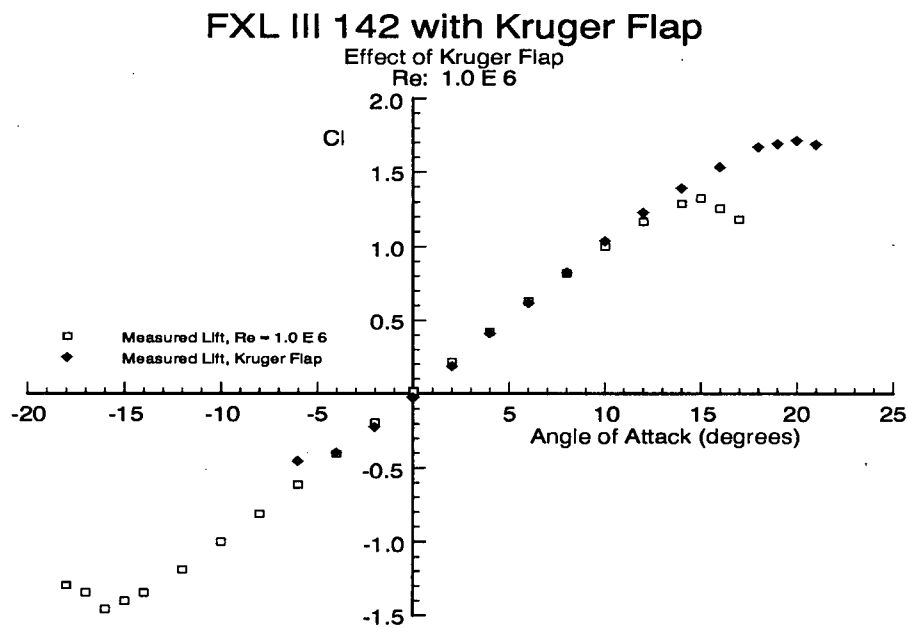
The experimental results are almost completely symmetric about 0, and line up almost perfectly with the previously published results. Again, the experimental stall angle is higher than might be expected, as the airfoil stalls at about 17° or 18°, compared with published stall angles of 14° to 16°. Both the published and experimental stalls are gentle.

Both clean airfoils behave well, and seem to be constructed correctly.

4.1.2 Effect of Kruger Flap

Kruger flaps are most commonly used on airfoils with a relatively sharp leading edge profile. Sharp leading edge airfoils usually have less drag, but they have a large suction spike which leads to a high pressure gradient near the leading edge. The large pressure gradient triggers stall at a lower angle of attack than a round nosed airfoil. When a Kruger flap is deployed, it increases $C_{l\,max}$ not only by adding a little chord to the airfoil, but also by effectively creating a rounder leading edge, reducing the suction spike. This is by far the leading cause of the increase in stall angle. The FXL airfoil model has a far sharper leading edge than the NACA, and so should be affected more by the addition of a flap. Airfoils with large leading edge radii also exhibit a more gentle stall, as seen on the clean NACA airfoils lift curve. This is the result of the airfoil undergoing trailing edge instead of leading edge stall. The NACA and FXL airfoils were chosen to provide a contrast between the performance of the models for two airfoils with differing stall characteristics.

Figures 4.3, 4.4, and 4.5 show the effect of adding a Kruger flap on the FXL's and NACA's respective lift curves.
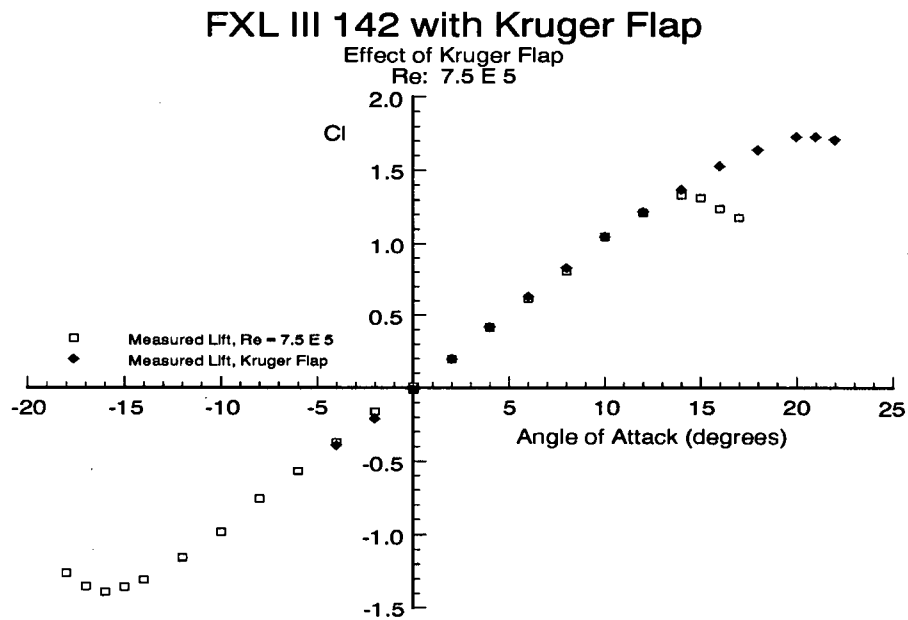
Figure 4.3: FXL III 142: effect of Kruger Flap on lift curve, Re = 7.5 E 5.

Figure 4.4: FXL III 142: effect of Kruger Flap on lift curve, Re = 1.0 E 6.

NACA 0018 with Kruger Flap
Effect of Kruger Flap
Re: 7.5 E 5

Cl

□ Measured Lift, Re - 7.5 E 5
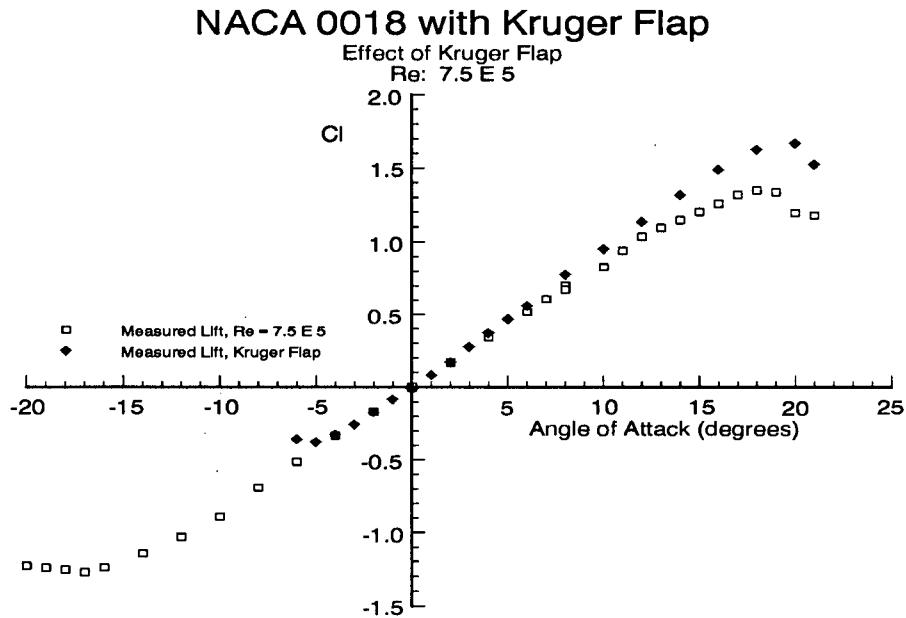◆ Measured Lift, Kruger Flap

Angle of Attack (degrees)

Figure 4.5: NACA 0018: effect of Kruger Flap on lift curve, Re = 7.5 E 5.

The results for the FXL are, as expected, virtually identical at both Reynolds numbers. Neither test reveals a significant change in lift curve slope. At Re = 7.5 E 5, the stall angle is increased from 14° to 20°, resulting in an increase in $C_{l\,max}$ from 1.33 to 1.73. At Re = 1.0 E 6, the increase in stall angle from 15° to 20° yields an increase in $C_{l\,max}$ from 1.33 to 1.72. The stall is also much gentler, as expected. The lift curves are no longer symmetrical, as at negative angles of attack the Kruger flap causes stall to occur far sooner, at about -4° or -5°. The flap has been effective.

Adding a Kruger flap to the NACA airfoil also delays stall, from 18° to 20° at Re = 7.5 E 5, increasing $C_{l\,max}$ by between 0.32 and 0.41. The change in $C_{l\,max}$ is not only due to the increase in stall angle, as was the case for the FXL airfoil. Most of the improvement results from improved airfoil performance at the higher angles of attack, as the lift curve remains nearly linear over a larger range. The clean airfoil already experienced trailing edge stall, and so no improvement in stall quality is expected or seen.

The NACA airfoil was also tested at two Reynolds numbers, Re = 3.7 E 5 and 7.5 E 5. Again, it would be needlessly repetitious to include both sets of data, as the results were similar. In

choosing which set to use, it is observed that this airfoil does not behave entirely inviscidly, despite having a linear lift curve, as the lift curve slope is around 0.088 to 0.095, below the ideal lift curve slope for an inviscid airfoil, 0.1096, or greater. The lift curve slope for the lower Reynolds number had the same form, but is a little lower, showing that the viscous effects are slightly larger. The same trend is seen in the pressure measurements, which are uniformly slightly lower at the lower Reynolds number. As the theoretical model assumes inviscid flow, it seems logical to compare the theoretical results with the data from the runs at Re = 7.5 E 5.

4.2 Pressure Distributions

The goal of the project was to measure pressure distributions along the Kruger flap equipped airfoils and compare them with the theoretical predictions. First, however, it must be verified that the pressure along the midspan line, where the taps are located, is not subject to tip effects or other examples of three-dimensional flow. This can be simply done by integrating the pressure results along the airfoil to obtain lift, which is then compared with the lift measured by the force balance. The integrated pressure lift curve should agree well with the measured lift, or, ideally, be slightly higher, as tip effects will decrease the measured lift. This was done for both airfoils, and the results are summarized in figures 4.6 and 4.7.

There is some error in the lift resulting from the integrated pressure measurements. As the pressure is only known at a finite number of points, the results are not actually integrated, but summed using Simpson's rule. This will result in slightly low values. Additionally, there are no pressure taps along the last two or three inches of the airfoils, which creates a small uncertainty in the calculated lift along this region.

The FXL results are in very good agreement, save for a single point on the integrated pressure curve at an 18° angle of attack, which can be explained as follows. A large amount of the lift generated by an airfoil at high angles of attack is the result of the suction peak, which refers to the very low pressures (large suction) on the first 30% or so of the upper surface. When the airfoil is close to stalling, the pressures in the suction peak can oscillate by significant
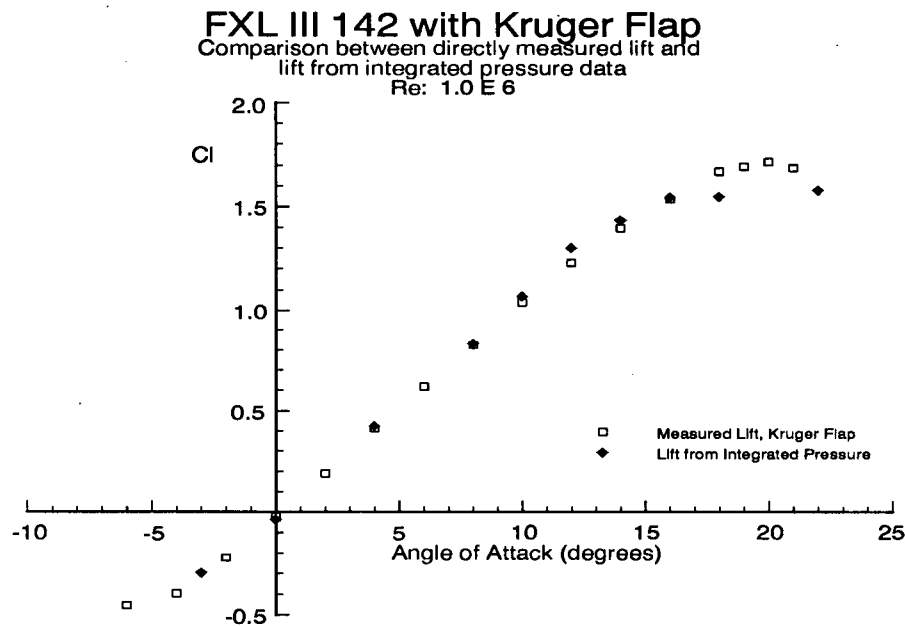
Figure 4.6: FXL III 142, verification of mid-span pressure.

amounts. When pressure is measured using a manometer, as was done in these measurements, it often takes a while for the readings to settle. If the readings are oscillating faster than the manometer can adjust, the manometer will tend to remain close to the last pressure measured. In the case of the suction peak, this would mean that the readings remain low, resulting in a lower integrated lift.

There are two slightly low points for the NACA airfoil, at 6° and 9°, which may be due either to a slight experimental error, or to the introduction of small three dimensional effects at these angles of attack. It is interesting to note that these points are also low for the data at Re $=$ 3.7 E 5.

Apart from the errors discussed, the integrated pressure measurements agree very well with the lift measurements.

NACA 0018 with Kruger Flap
Comparison between directly measured lift and lift from integrated pressure data
Re: 7.5 E 5
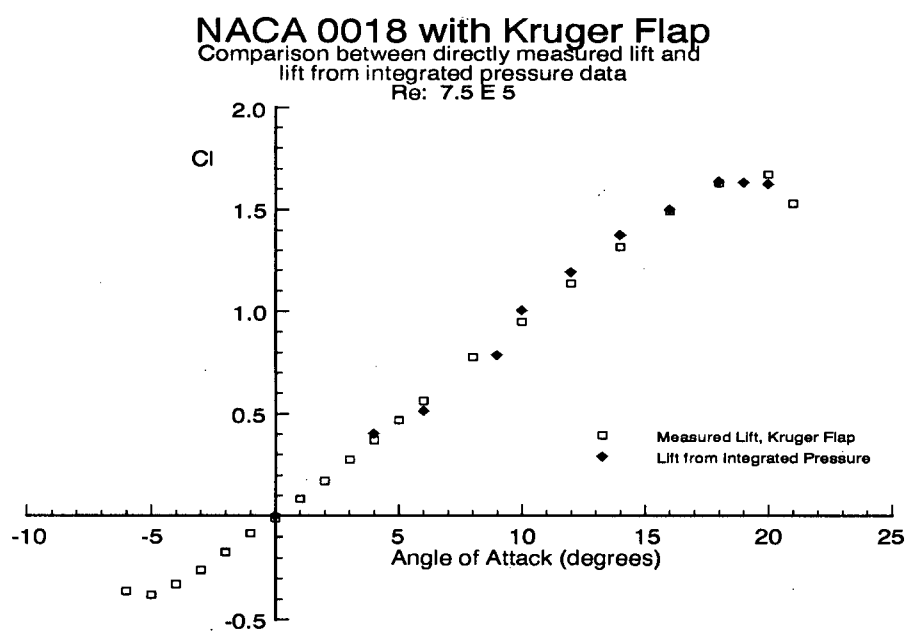
Figure 4.7: NACA 0018, verification of mid-span pressure.

4.2.1 NACA 0018 and FXL III 142 Airfoil Pressure Distributions

The sheer volume of data taken prohibits including all of the angles of attack measured. Only the results for the representative angles 0°, 4°, 8°, 9°, 12°, 16°, and 22° are shown. The pressure distribution for each angle of attack is compared to the distribution predicted by each of the four different models, except for the 16° and 22° cases, where some of the models would not reliably converge.

Low Angles of Attack: 0° and 4°

At low angles of attack, none of the models performs exceptionally well. A large suction spike exists just before separation. This spike is reduced as angle of attack increases, and is smallest for the radial doublet model. Agreement is satisfactory along the suction surface, and again improves as angle of attack increases. The separation bubble seems to have little effect on the suction surface pressure distribution. The pressure surface agreement is also acceptable, except in the separation bubble region. Single doublet and source and sink model results are almost identically poor, predicting a separation bubble of higher pressure than the rest of the pressure surface. The two doublet model doesn't fair significantly better. The radial doublet performs best, predicting the bubble pressure distribution well at 0°, and as well as any of the others at higher angles of attack. Overall, agreement is poor at low angles of attack.
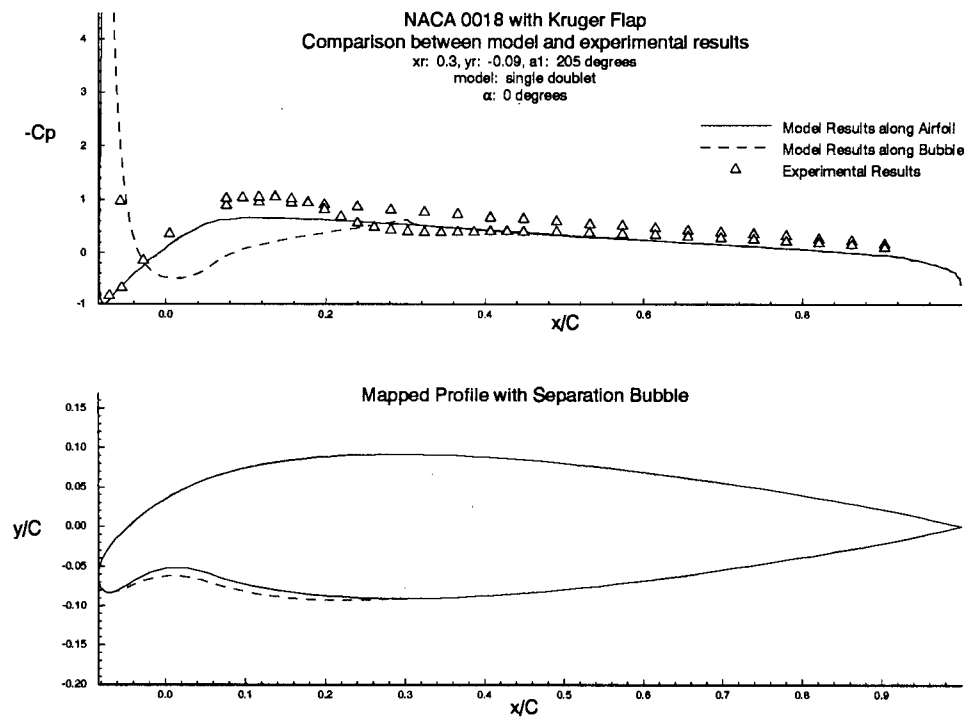
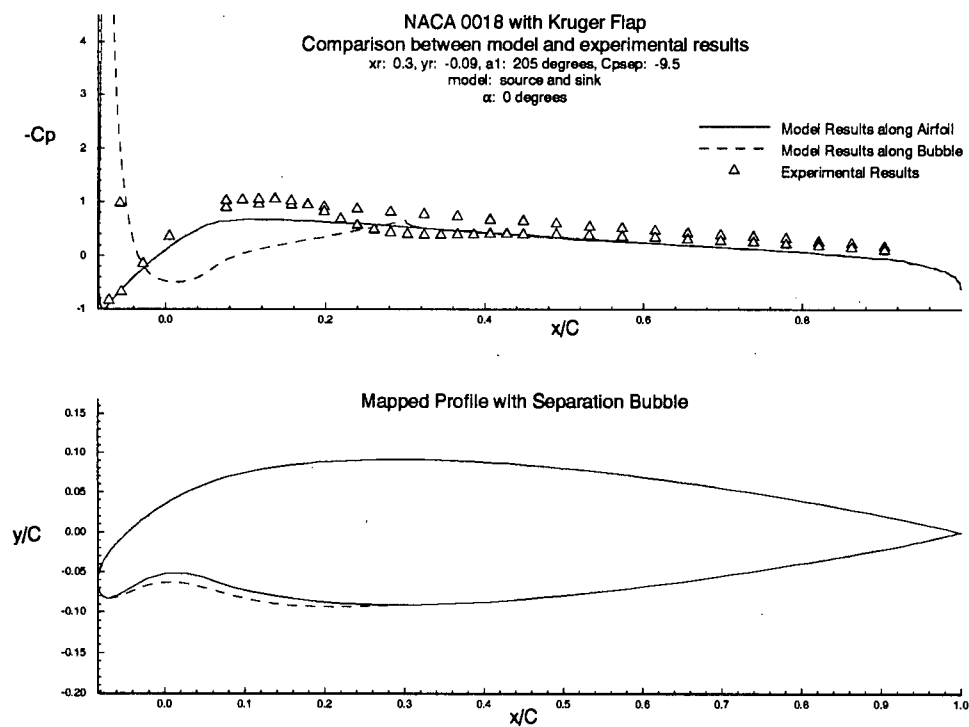Figure 4.8: NACA 0018, 0 degrees, single doublet model

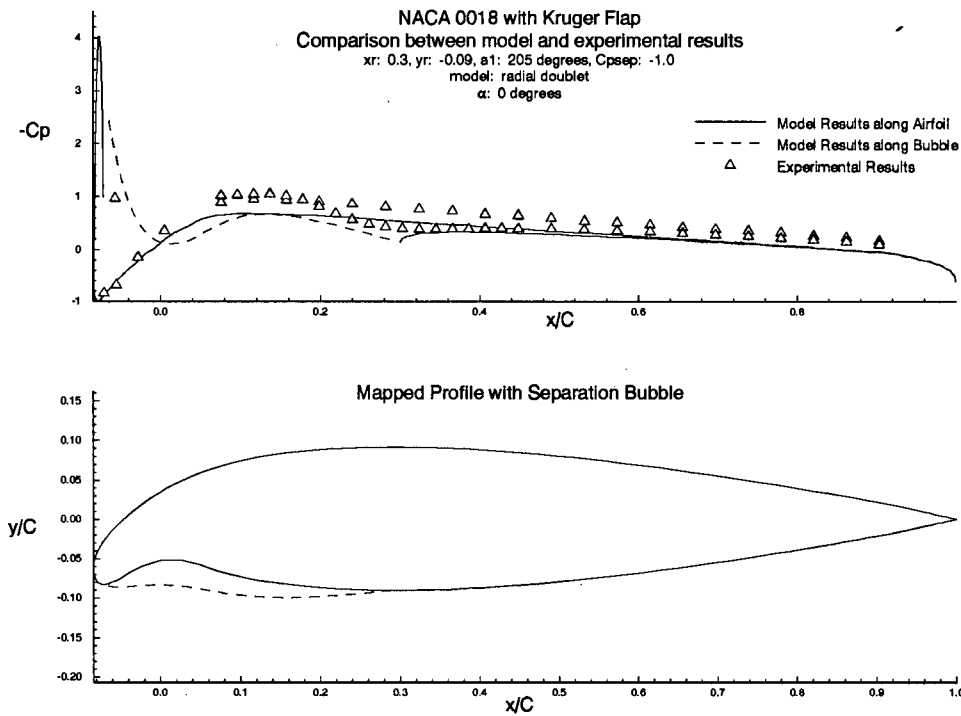Figure 4.9: NACA 0018, 0 degrees, source and sink model

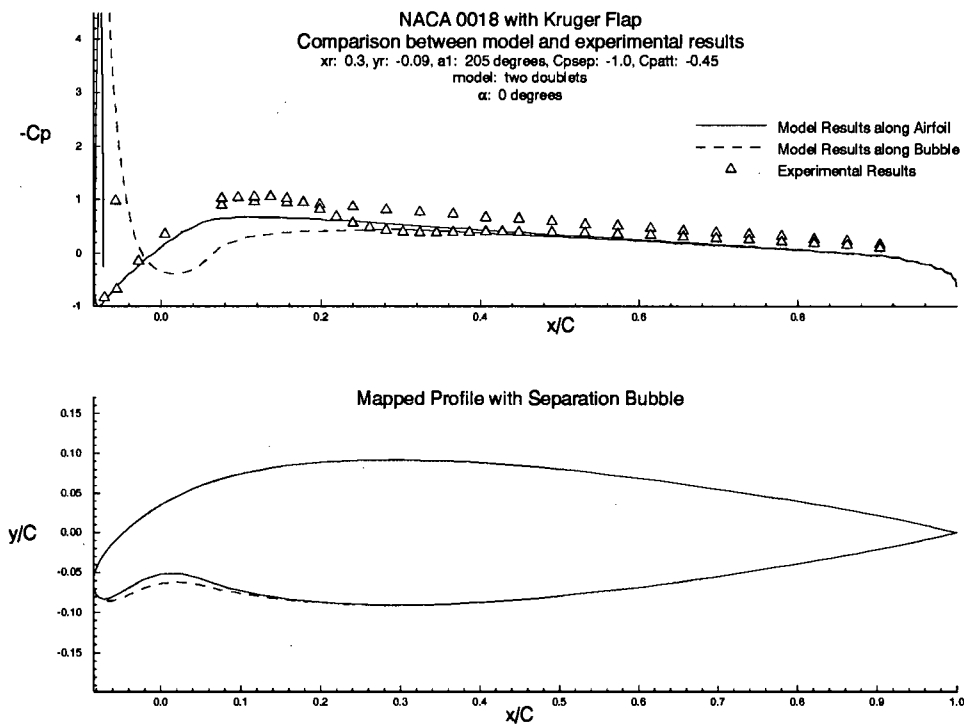Figure 4.10: NACA 0018, 0 degrees, radial doublet model

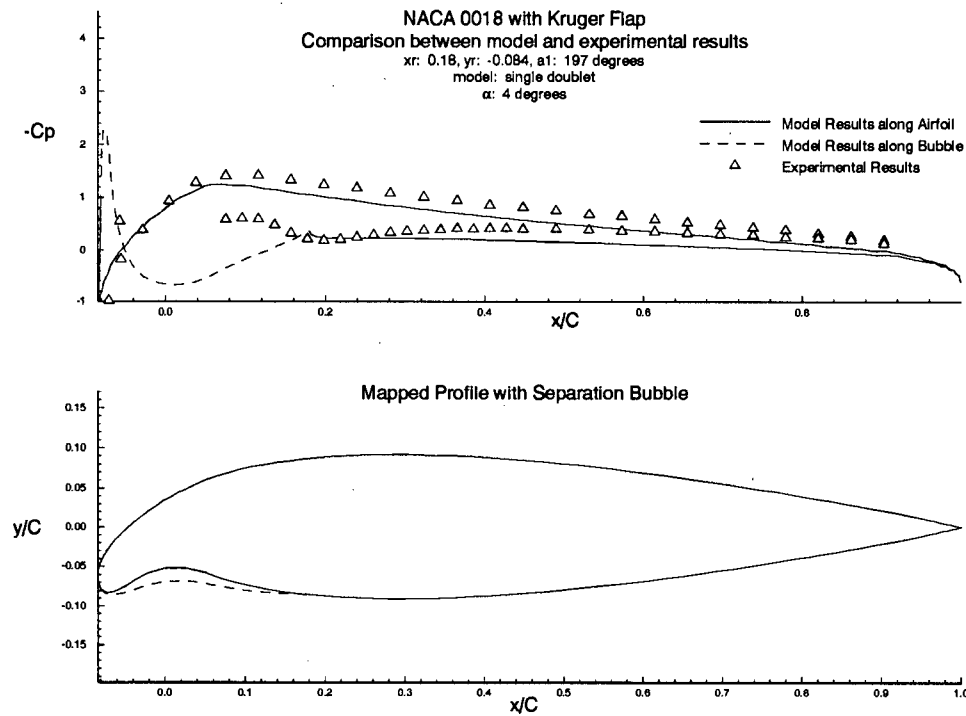Figure 4.11: NACA 0018, 0 degrees, two doublets model

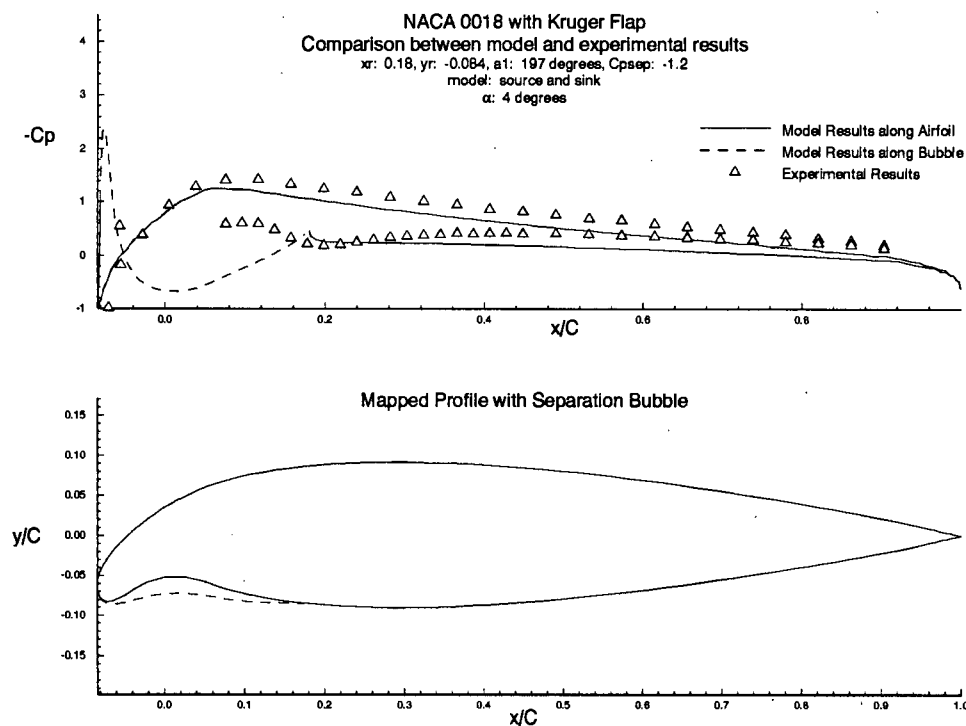Figure 4.12: NACA 0018, 4 degrees, single doublet model

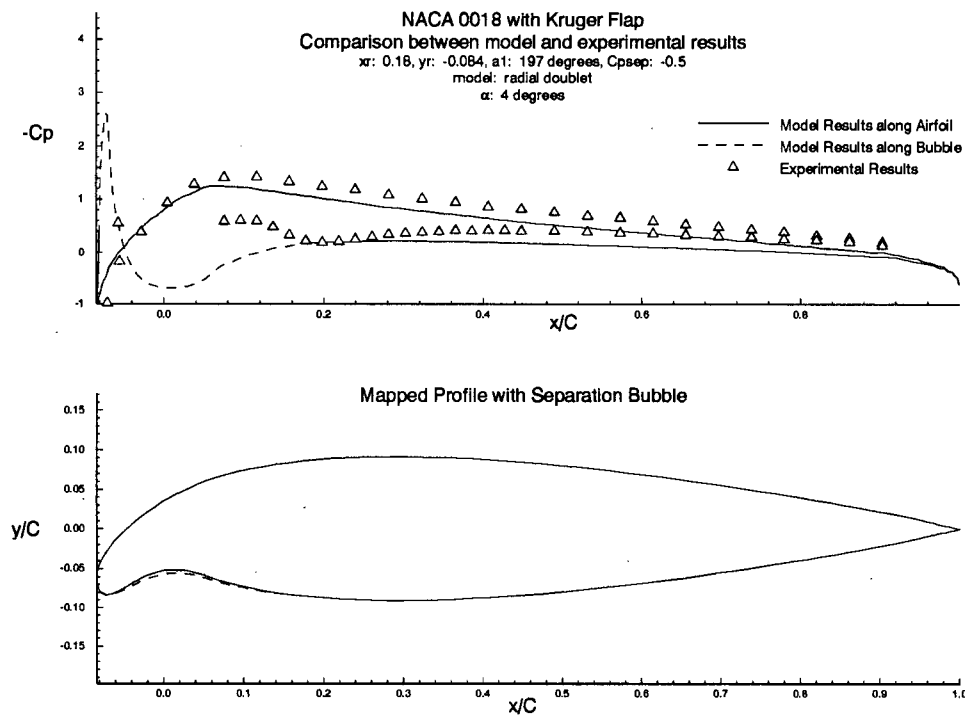Figure 4.13: NACA 0018, 4 degrees, source and sink model

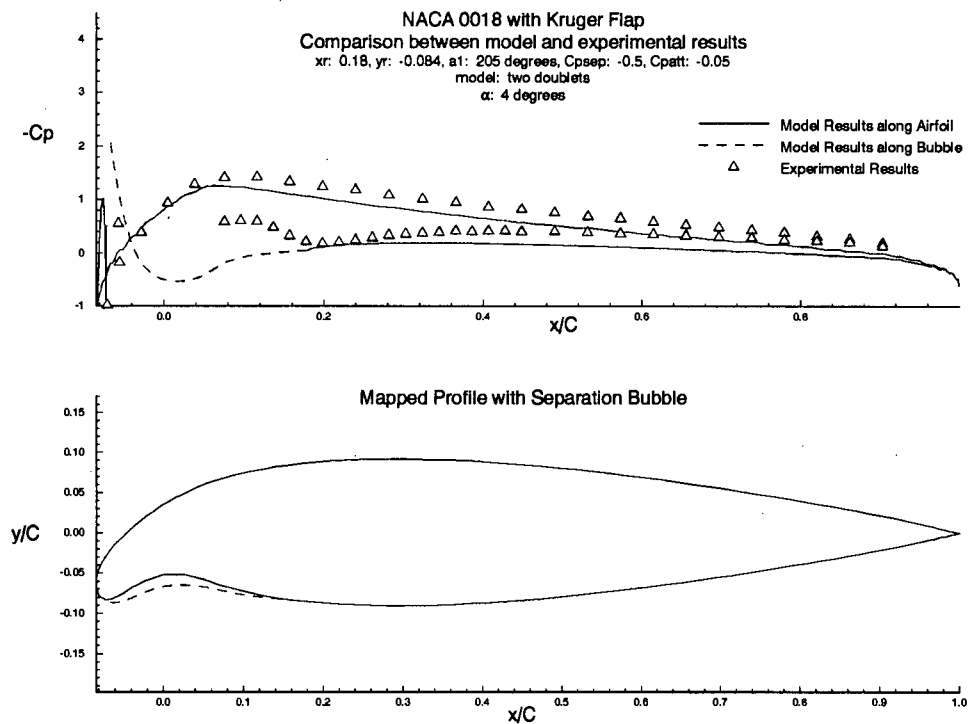Figure 4.14: NACA 0018, 4 degrees, radial doublet model

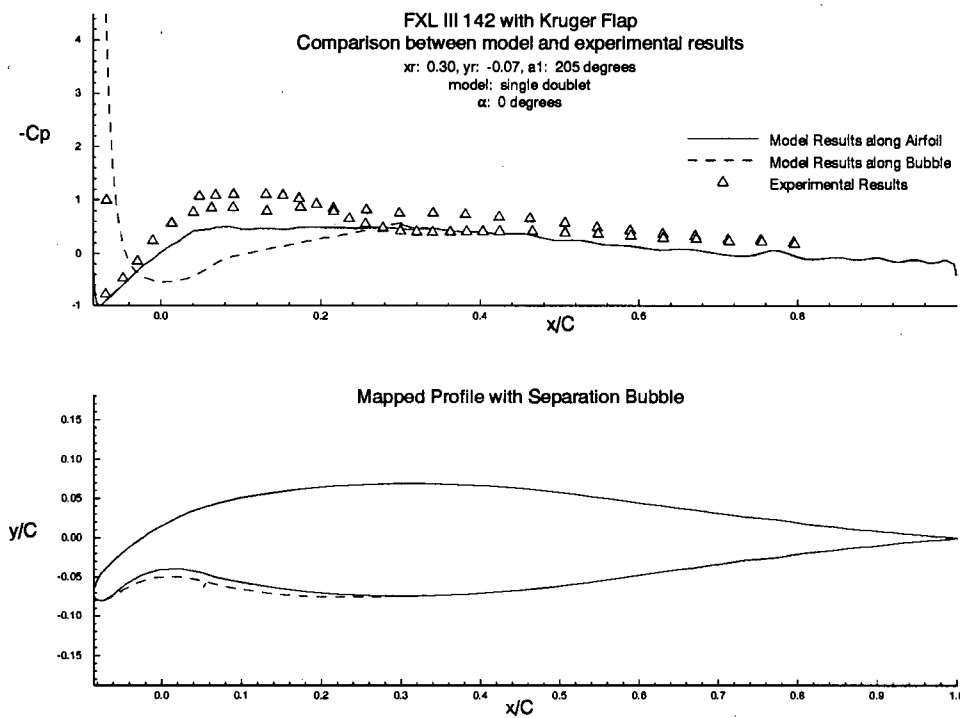Figure 4.15: NACA 0018, 4 degrees, two doublets model

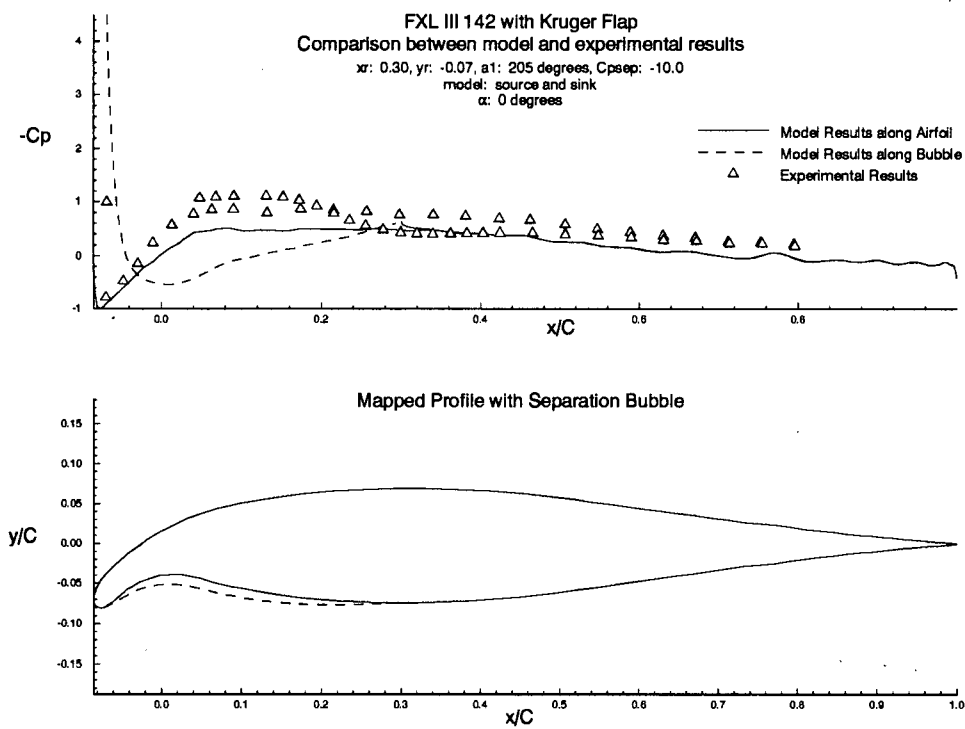Figure 4.16: FXL III 142, 0 degrees, single doublet model

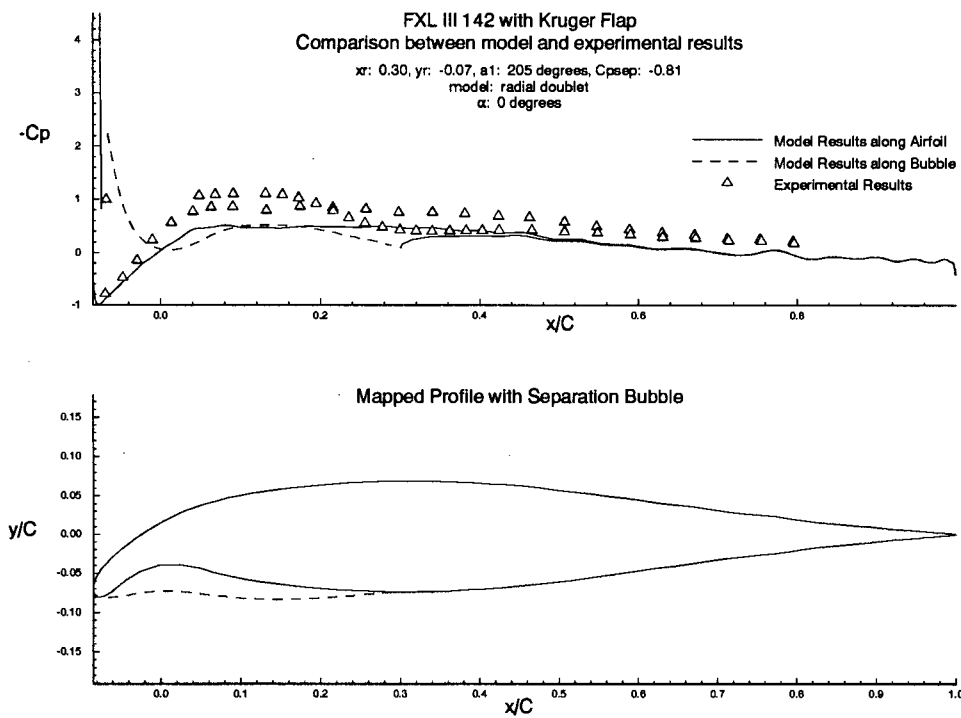Figure 4.17: FXL III 142, 0 degrees, source and sink model

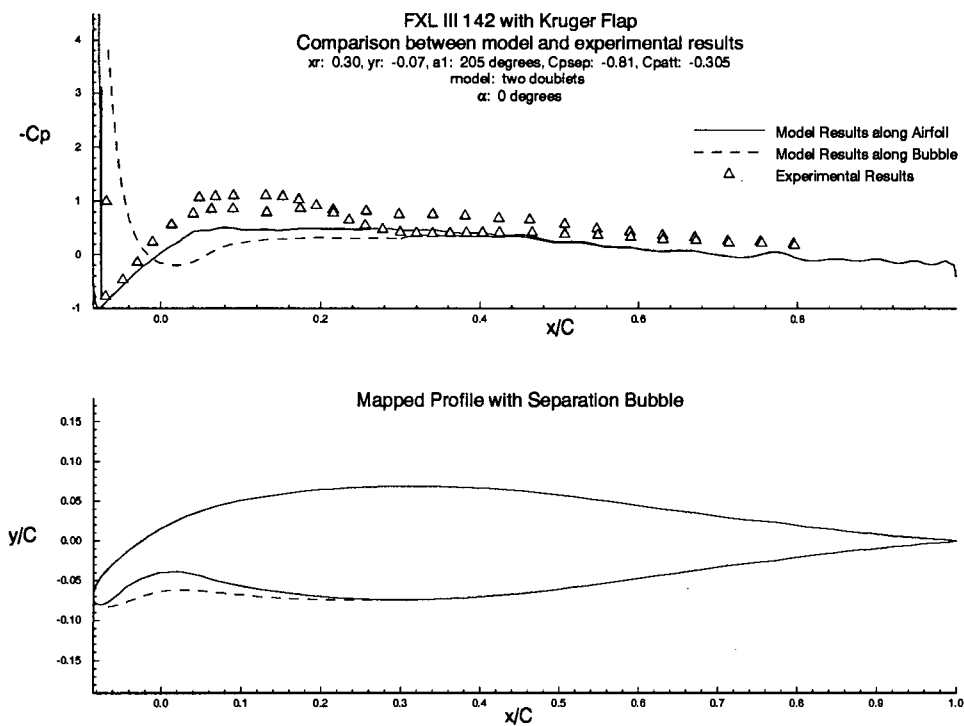Figure 4.18: FXL III 142, 0 degrees, radial doublet model

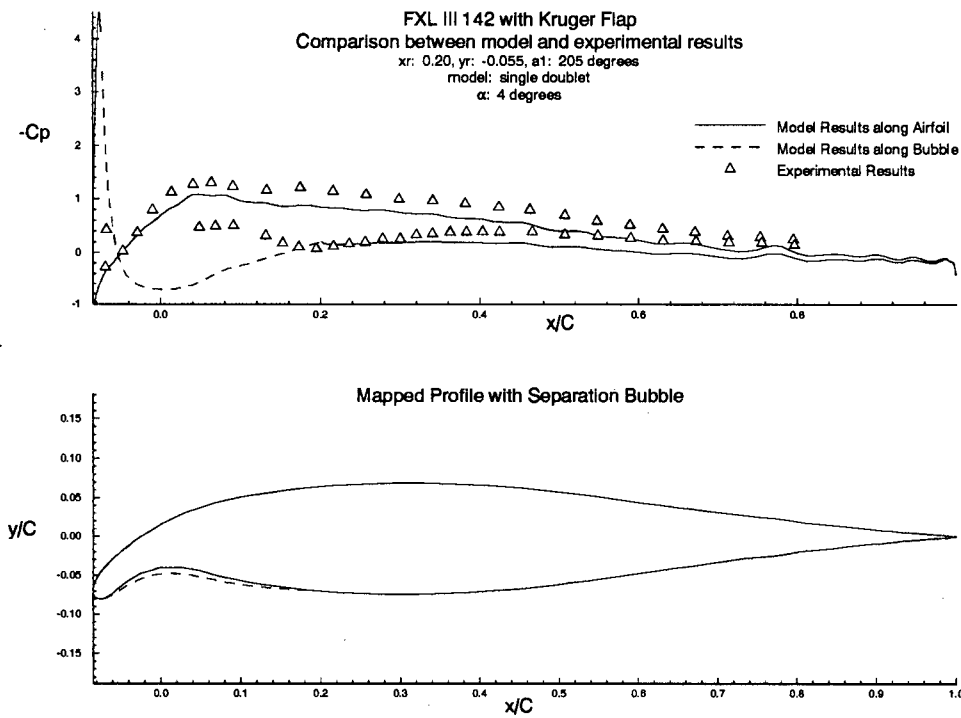Figure 4.19: FXL III 142, 0 degrees, two doublets model

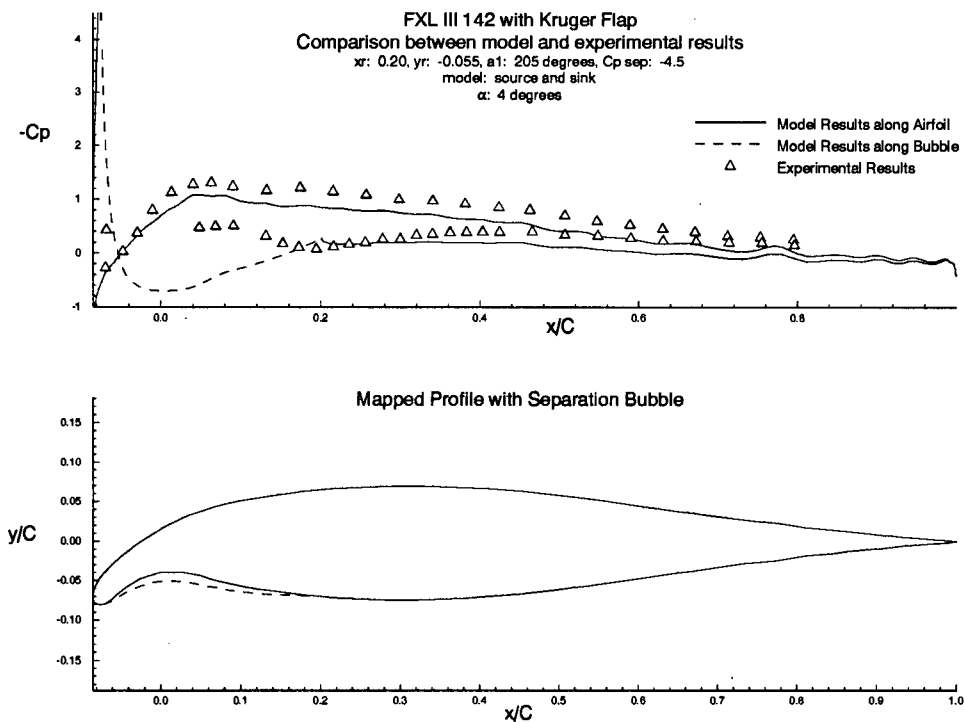Figure 4.20: FXL III 142, 4 degrees, single doublet model

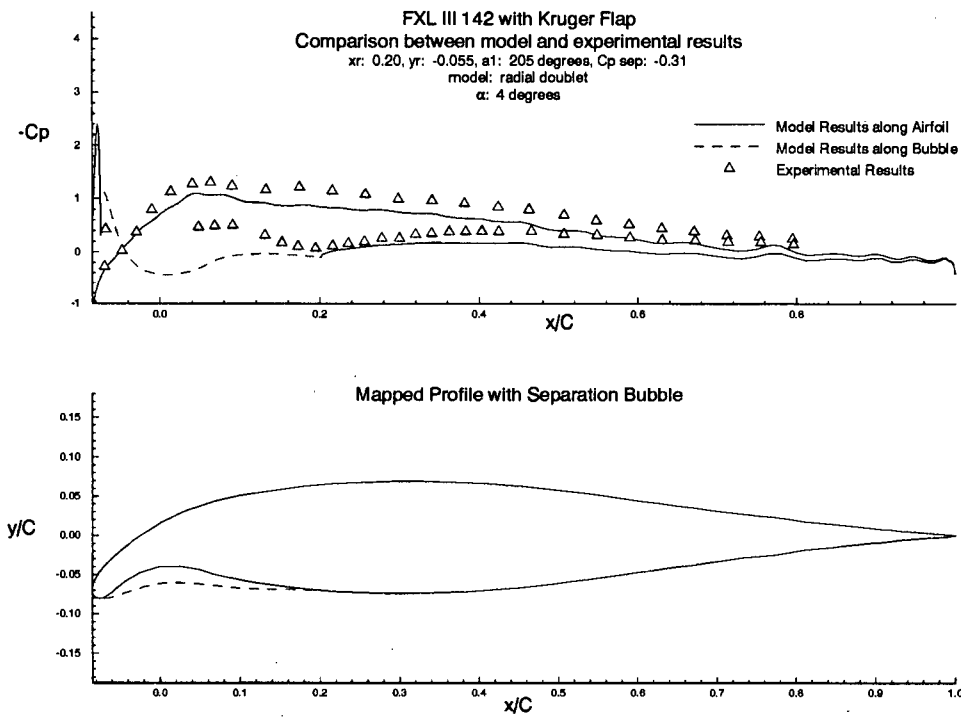Figure 4.21: FXL III 142, 4 degrees, source and sink model

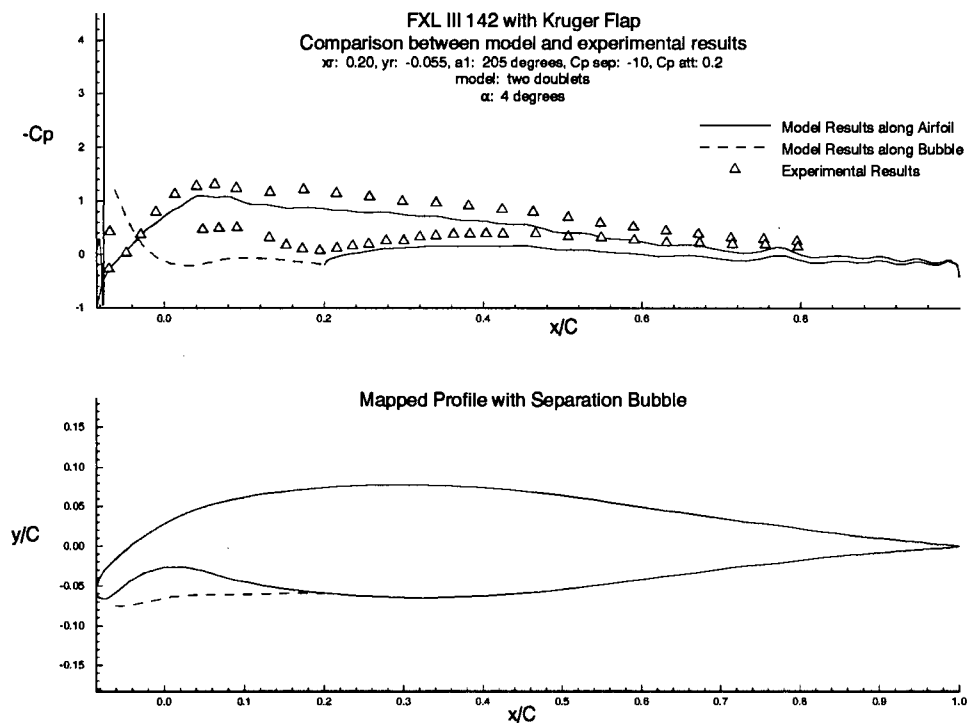Figure 4.22: FXL III 142, 4 degrees, radial doublet model

Figure 4.23: FXL III 142, 4 degrees, two doublets model

Mid Range Angles of Attack: 8°, 9°, and 12°

The limited success of the models at lower angles of attack is not of great importance. When the flap is deployed, the aircraft will typically be either taking off or landing, and therefore be traveling at a higher angle of attack. This means that the range of angles from about 8° to 14° is really where the most accuracy is needed.

Angles of attack of 9° and 12° degrees for the NACA 0018, and 8° and 12° degrees for the FXL III 142 airfoil were chosen as representative. Good agreement is seen on the suction surface for both airfoils. The models overestimate the first part of the suction peak on the both airfoils, which is to be expected, as the flow model neglects the effects of viscosity. In the first section of the suction peak, the pressure and velocity gradients are largest, and so are the effects of viscosity. This effect is minimal on the FXL airfoil, which had a nearly ideal lift curve, but larger on the NACA, whose lift curve was significantly lower than ideal.

On the pressure side, the single doublet model does poorly at first, but improves as the angle of attack increases. The other three models, which use the separation pressure coefficient as a boundary condition, meet with limited success at 8° and 9°. They show the first bit of a low pressure bubble, but this rapidly decays back to a higher pressure.

By 12°, all models are performing well, a trend which continues until around 16°, where the proximity to stall starts reducing lift. Indeed, the results of the models are almost identical. This is partly a result of the inputs to the models, as will be discussed later. Agreement along the suction surface is very good, and along the pressure surface the models are also doing well.

The source and sink model has some problems at these angles of attack. It has developed a "saucer" shape pressure distribution for the NACA profile at 12°. This is a result of the model trying to match the imposed separation pressure condition. It does succeed, but not in an empirically acceptable fashion. If the separation pressure condition is relaxed to $C_{p\,sep}=0.7$ or so, this model yields results very similar to the others.

One interesting feature becomes apparent at these angles. On the FXL airfoil, a dip in $-C_p$ just

prior to the suction peak becomes apparent. This dip first appears at around 8°, and increases in size with angle of attack. This effect is present in both the experimental and theoretical data. It seems to be a result of the large changes in curvature in the flap profile near the leading edge. The NACA airfoil, with its larger leading edge radius, and smaller changes in curvature near the leading edge, doesn't exhibit the same effect until much later, at around 14° or 16°.

Figure 4.24: NACA 0018, 9 degrees, single doublet model
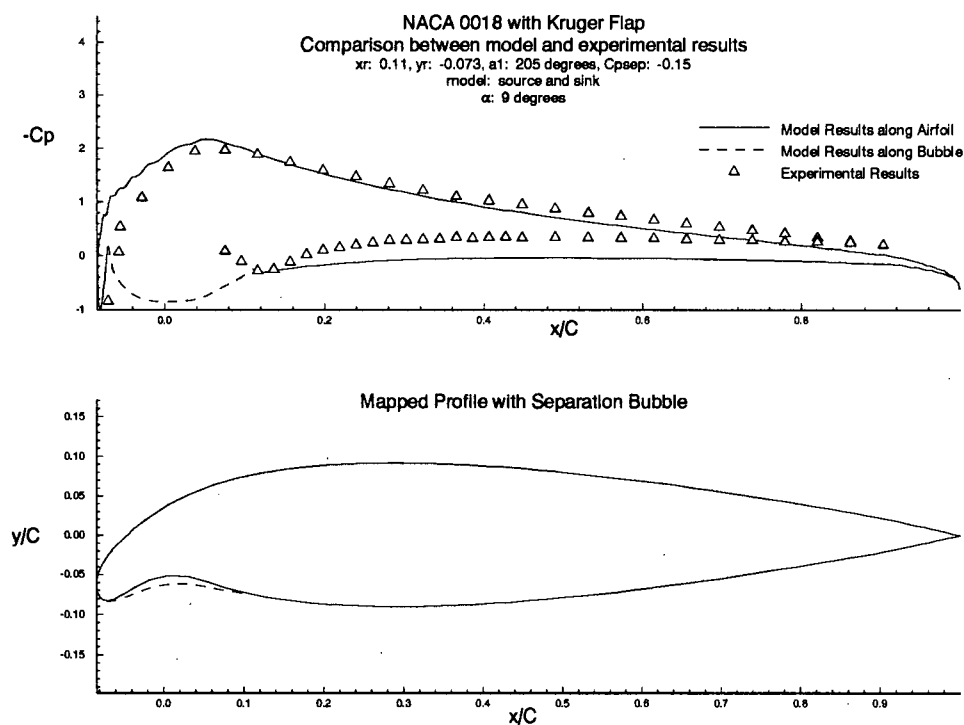
Figure 4.25: NACA 0018, 9 degrees, source and sink model
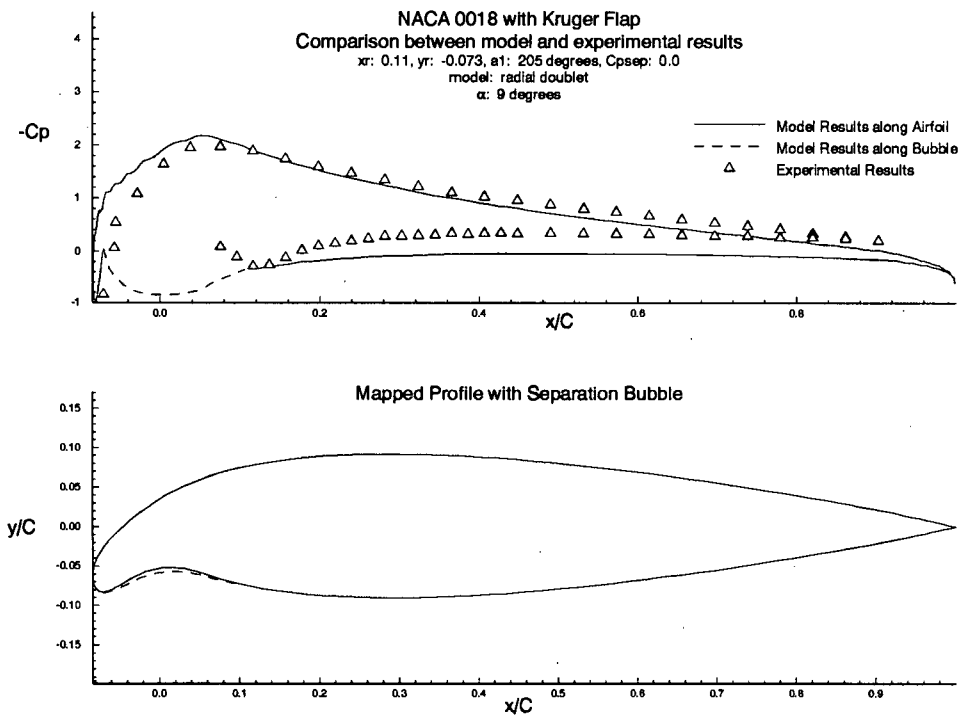
Figure 4.26: NACA 0018, 9 degrees, radial doublet model

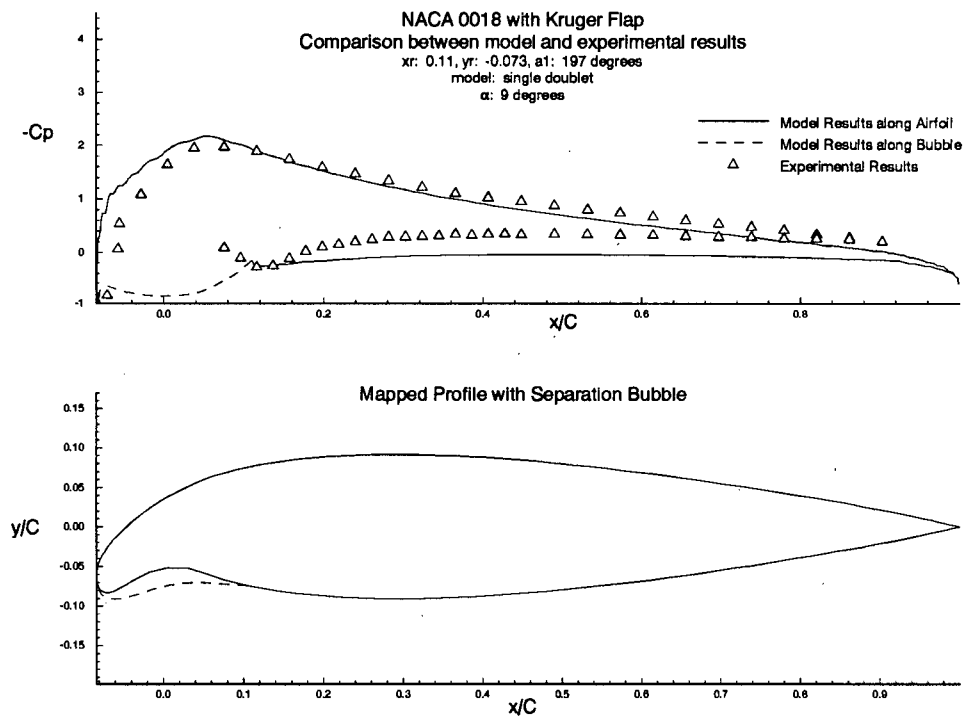Figure 4.27: NACA 0018, 9 degrees, two doublets model

Figure 4.28: NACA 0018, 12 degrees, single doublet model

Figure 4.29: NACA 0018, 12 degrees, source and sink model
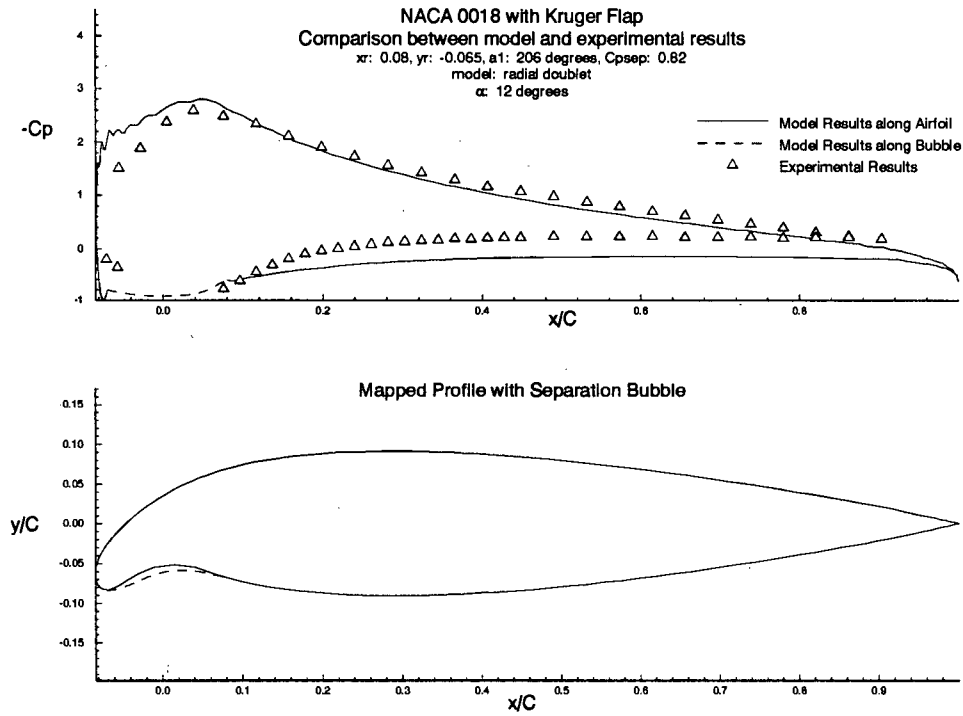
Figure 4.30: NACA 0018, 12 degrees, radial doublet model

Figure 4.31: NACA 0018, 12 degrees, two doublets model

Figure 4.32: FXL III 142, 8 degrees, single doublet model

Figure 4.33: FXL III 142, 8 degrees, source and sink model

Figure 4.34: FXL III 142, 8 degrees, radial doublet model

Figure 4.35: FXL III 142, 8 degrees, two doublets model

Figure 4.36: FXL III 142, 12 degrees, single doublet model

Figure 4.37: FXL III 142, 12 degrees, source and sink model

Figure 4.38: FXL III 142, 12 degrees, radial doublet model
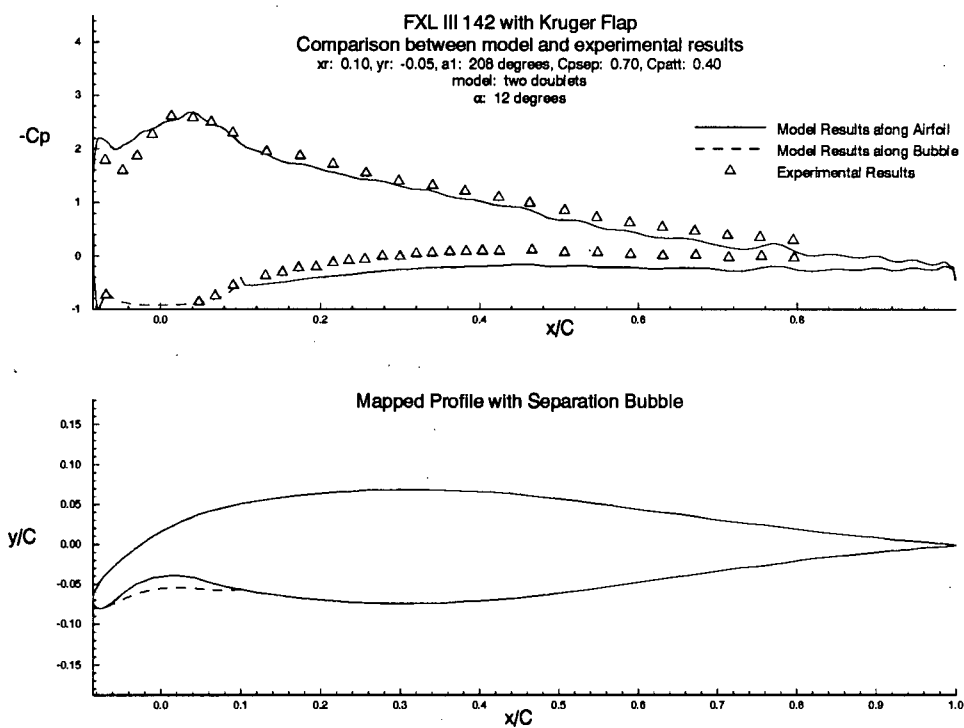
Figure 4.39: FXL III 142, 12 degrees, two doublets model

High Angles of Attack: 16° and 22°

As the airfoils approach stall, both non-linear and viscous effects on pressure distribution and lift become apparent. There isn't much of a difference in the pressure distribution between the models. They all overpredict the values in the suction peak and along the pressure side of the airfoil. The dip in the pressure distribution discussed in the previous section has developed into a large suction spike in the FXL airfoil solutions. A similar, but smaller, spike also appears in the pressure distribution along the NACA airfoil. Happily, the models all behave well in the separation bubble region. The models successfully predict the shape of the pressure distribution, but are no longer quite as good at predicting its magnitude.

In general, it becomes more difficult for the models to converge as the angle of attack increases. The sensitivity of the models to the boundary conditions is increased, particularly for the two doublet model, which has problems converging for the NACA airfoil at angles of attack larger than about 15°, or for the FXL airfoil for angles greater than 18°. For this reason, the figure for the NACA airfoil with the two doublet model at 16° is not included.

Both Kruger flap equipped airfoils experience trailing edge stall, as shown for the FXL III 142 at 22° in figure 4.47. None of the models will converge for an angle of attack this high, and so the results from the single doublet model at 16° are included for reference. The results would have been meaningless in any case, as potential flow solutions cannot predict stall.
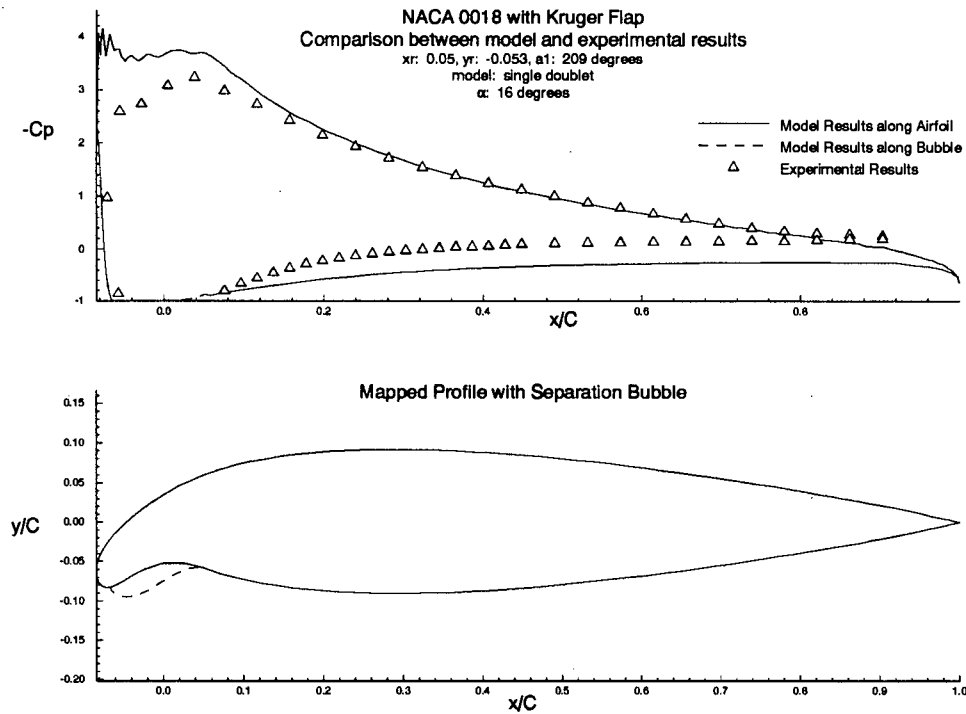
Figure 4.40: NACA 0018, 16 degrees, single doublet model

Figure 4.41: NACA 0018, 16 degrees, source and sink model
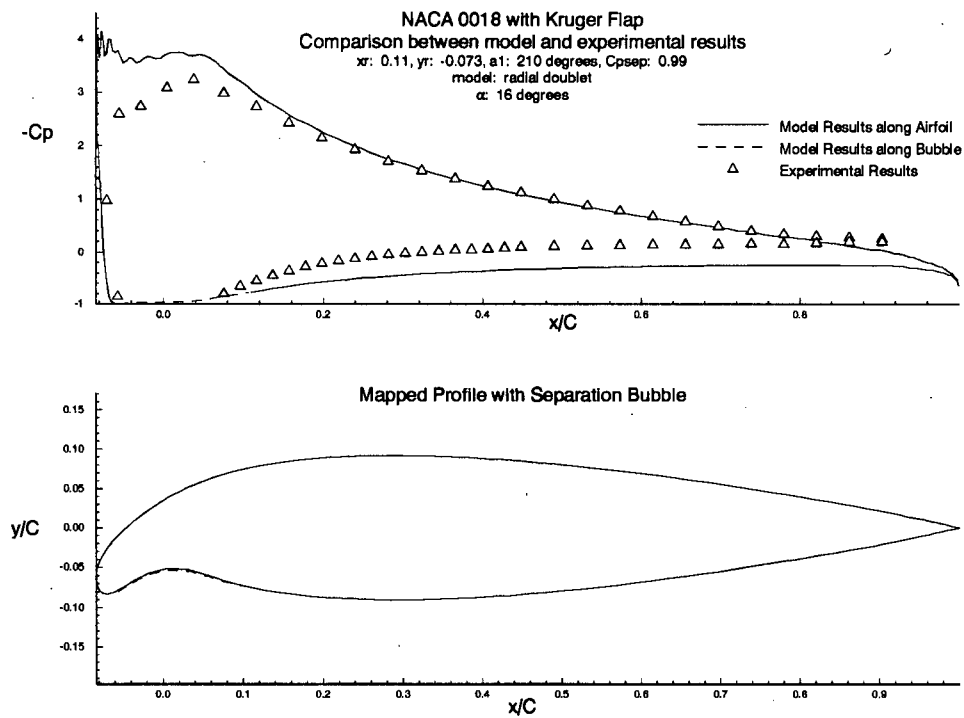
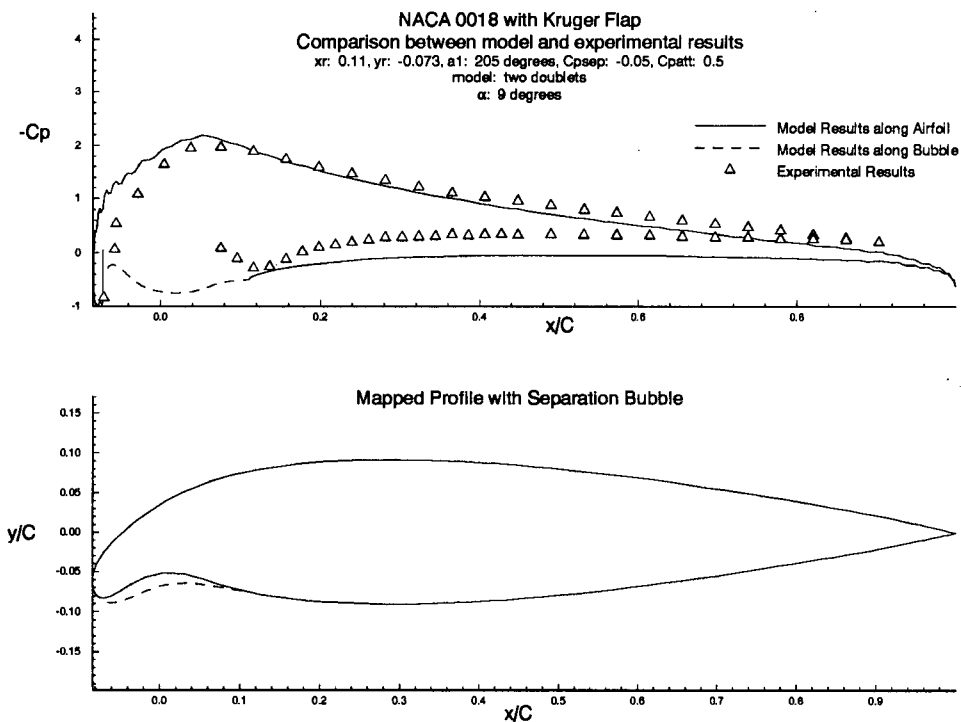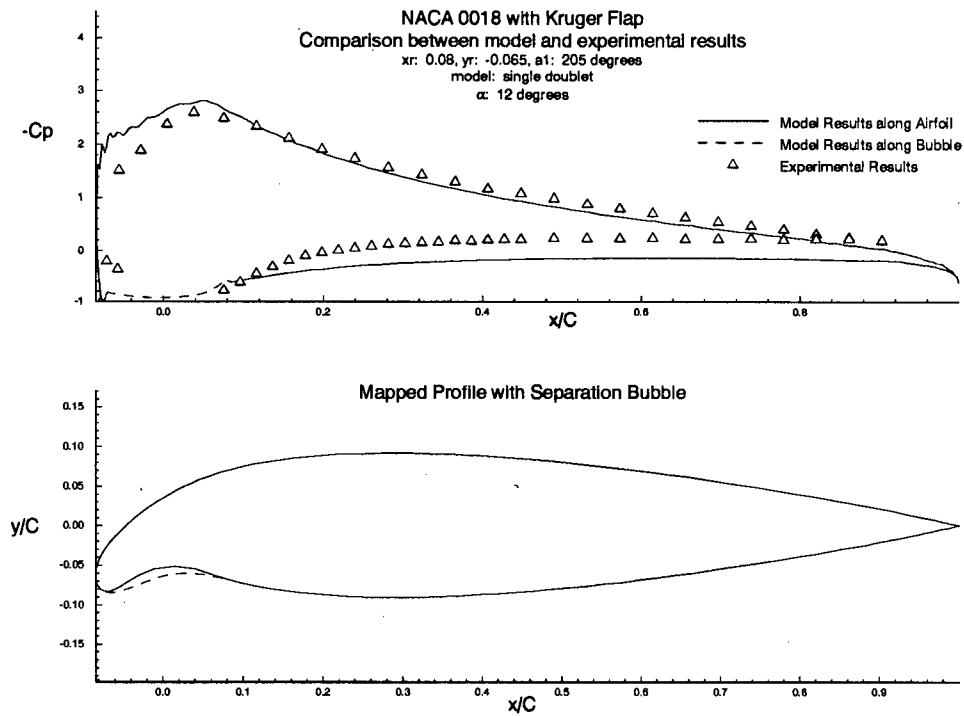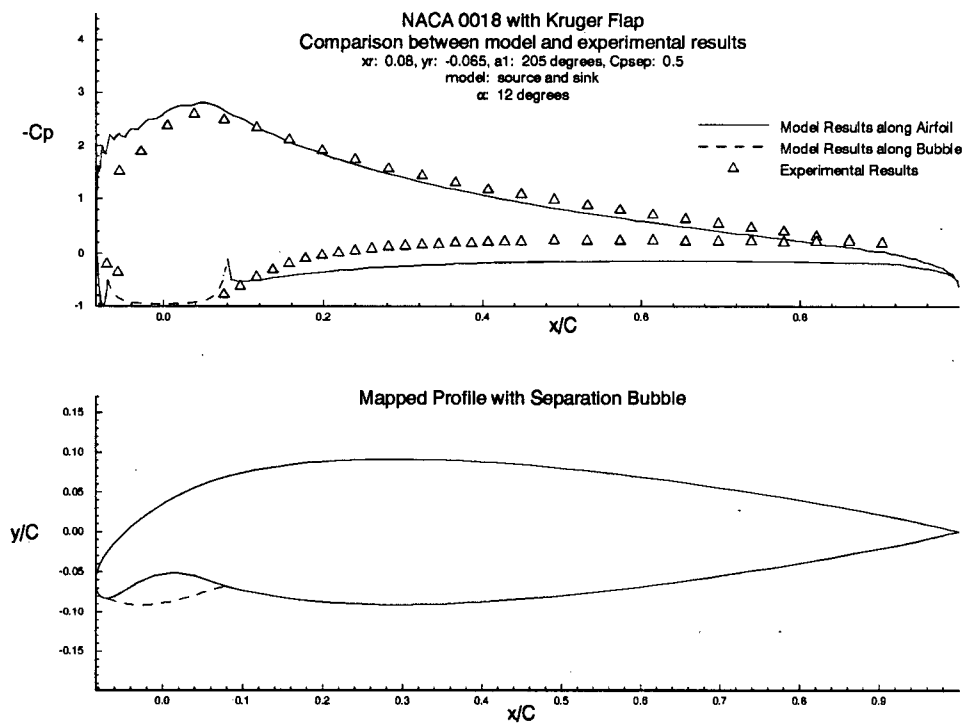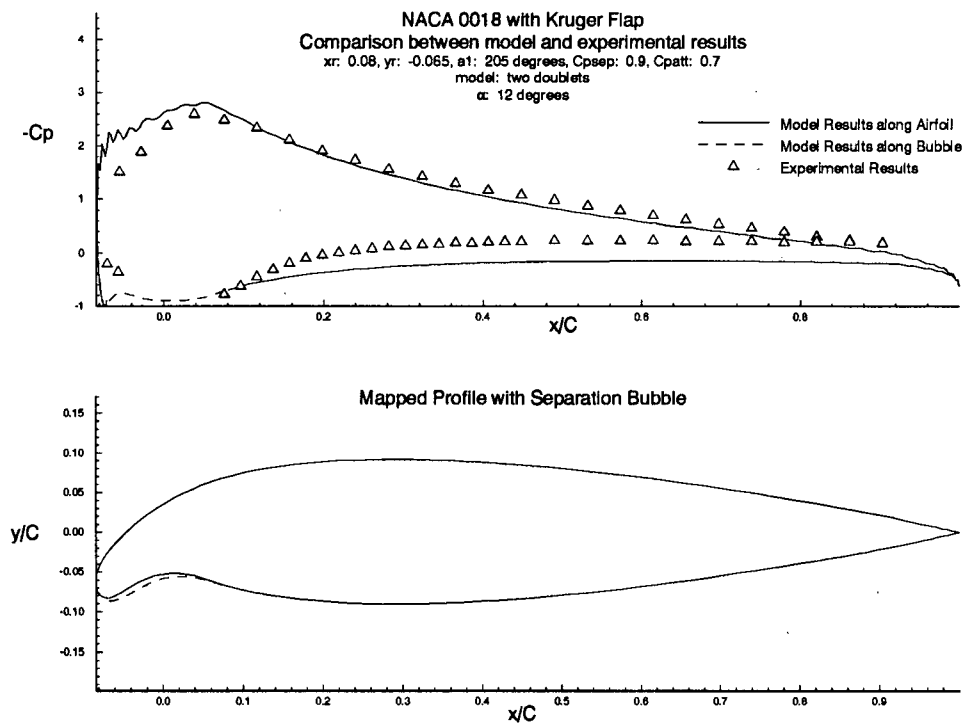Figure 4.42: NACA 0018, 16 degrees, radial doublet model
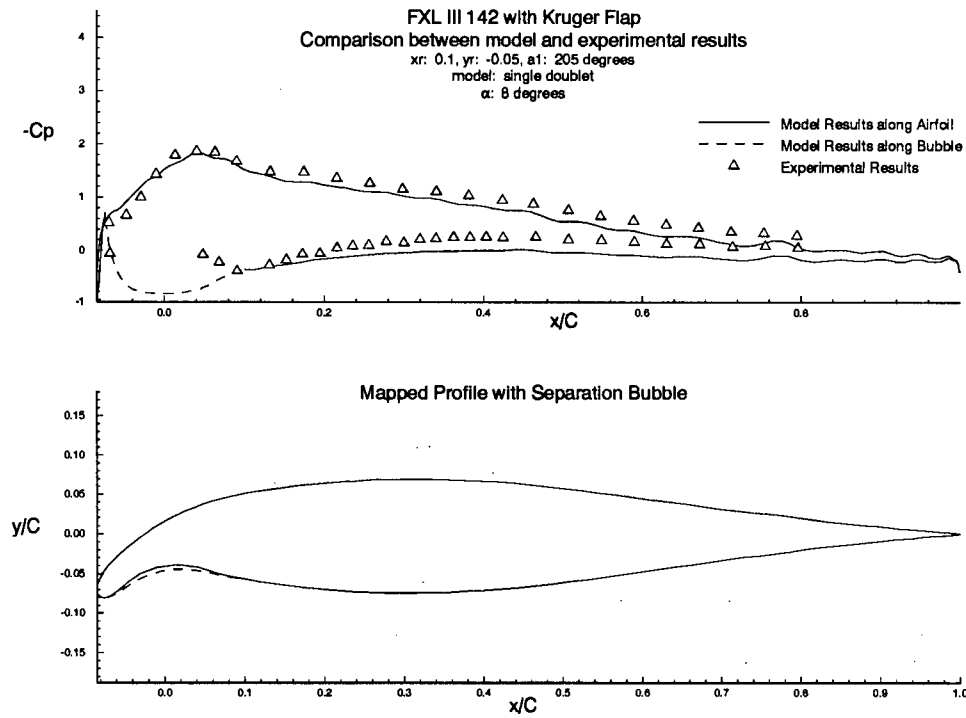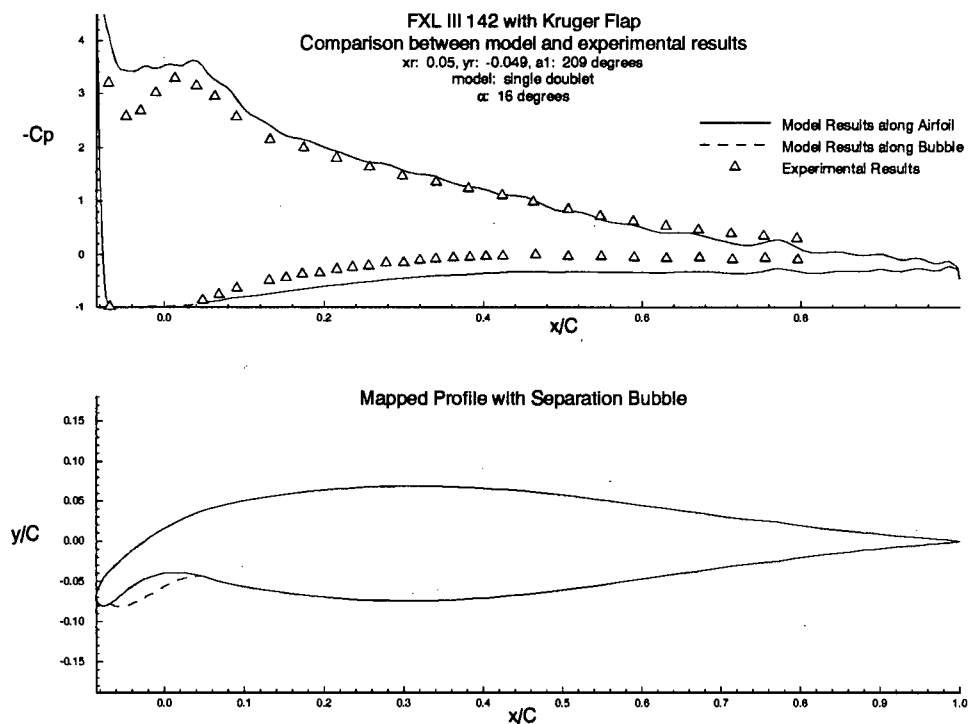

Figure 4.43: FXL III 142, 16 degrees, single doublet model
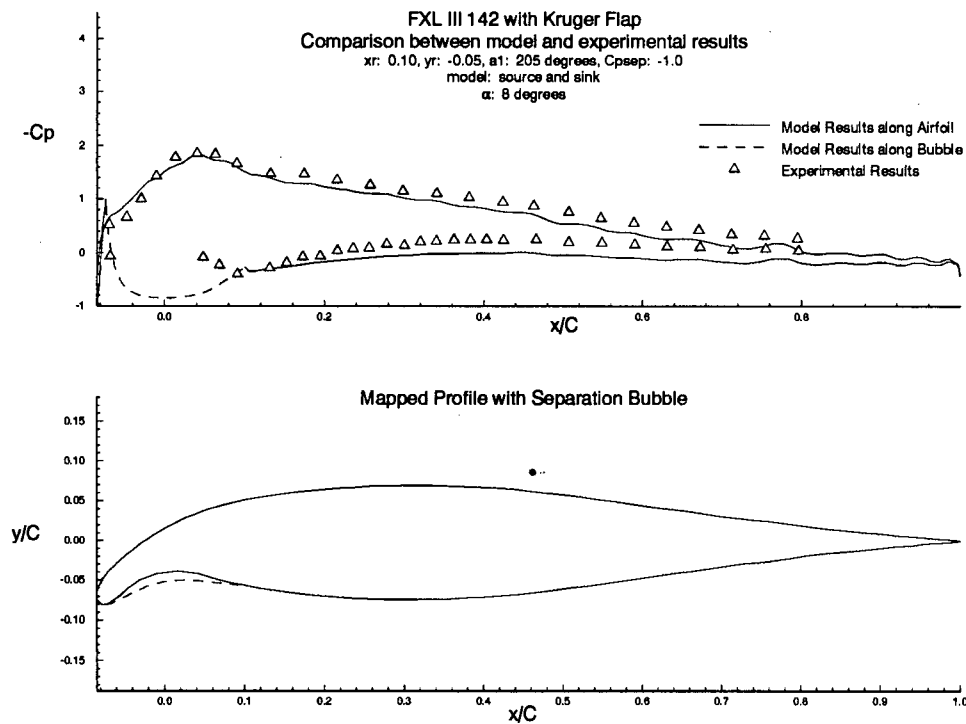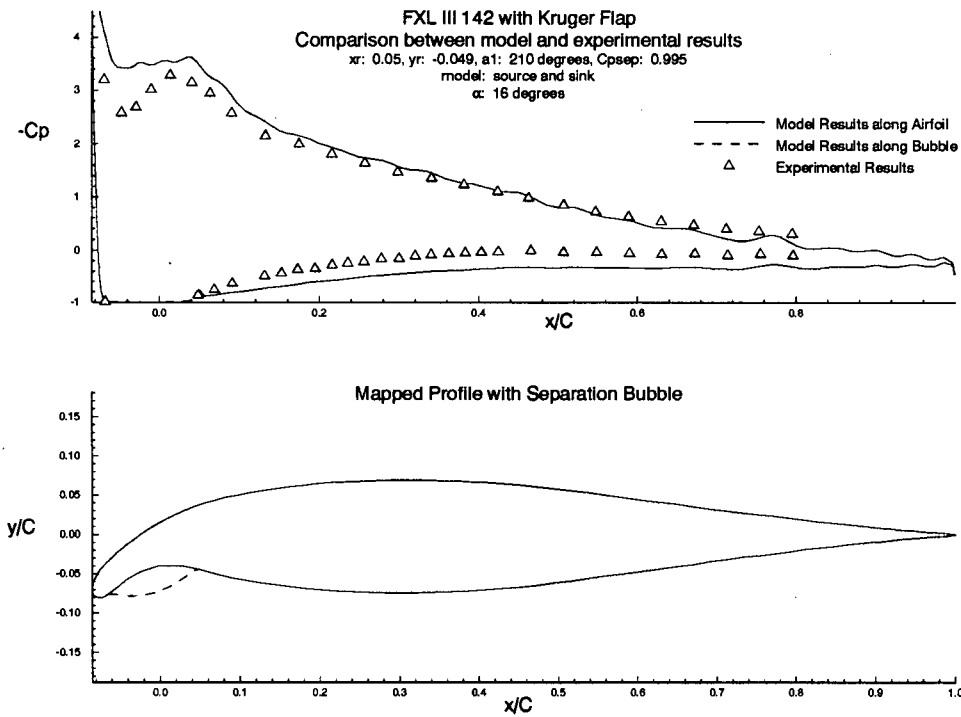
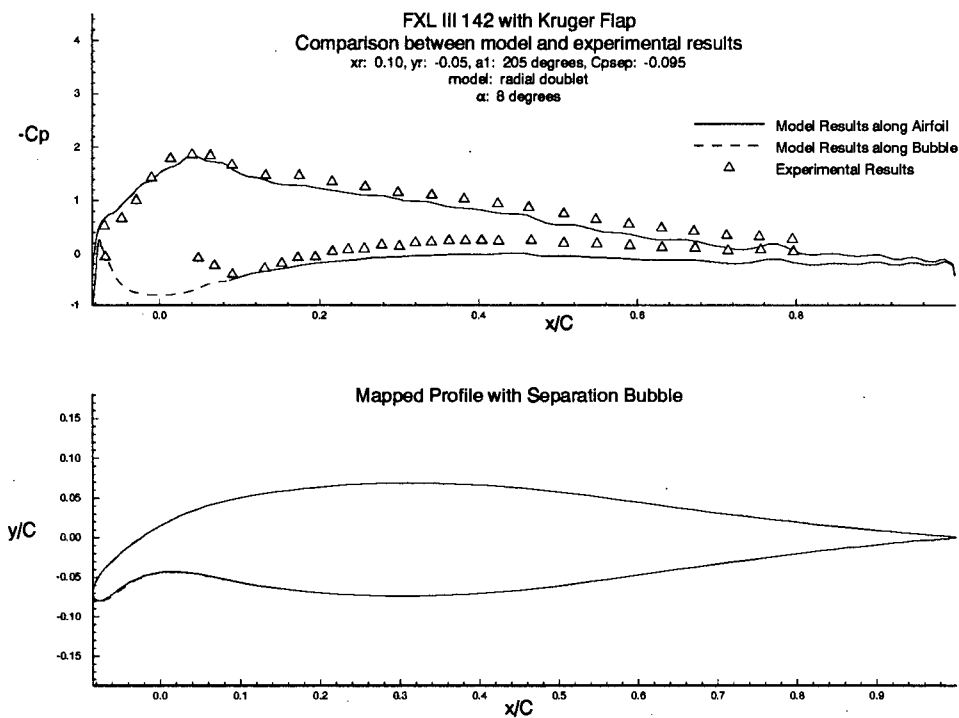Figure 4.44: FXL III 142, 16 degrees, source and sink model

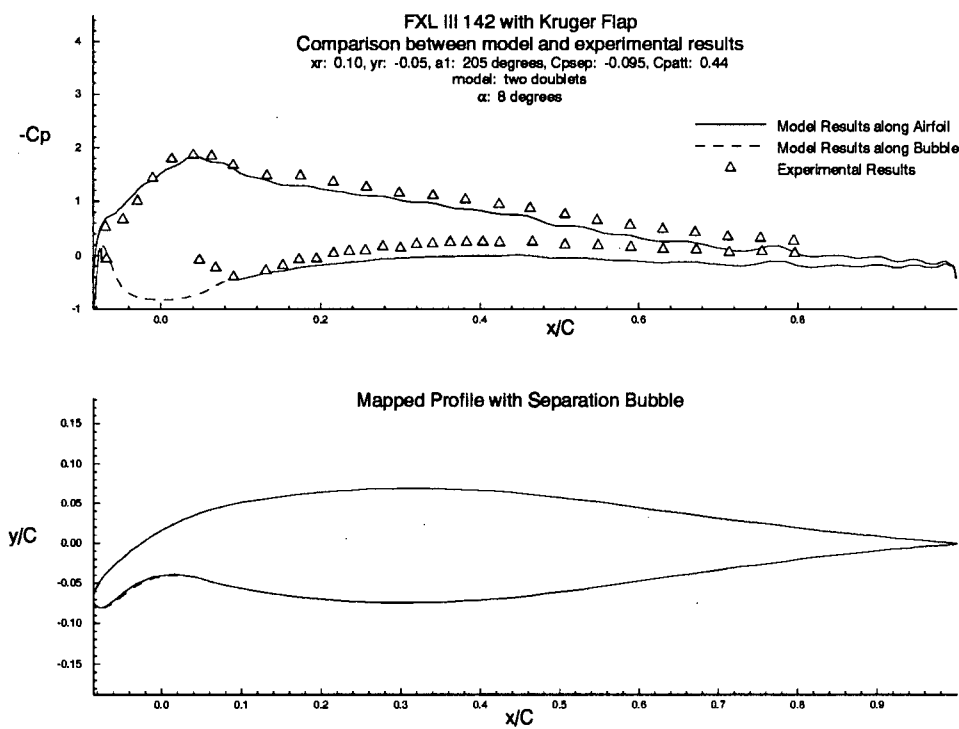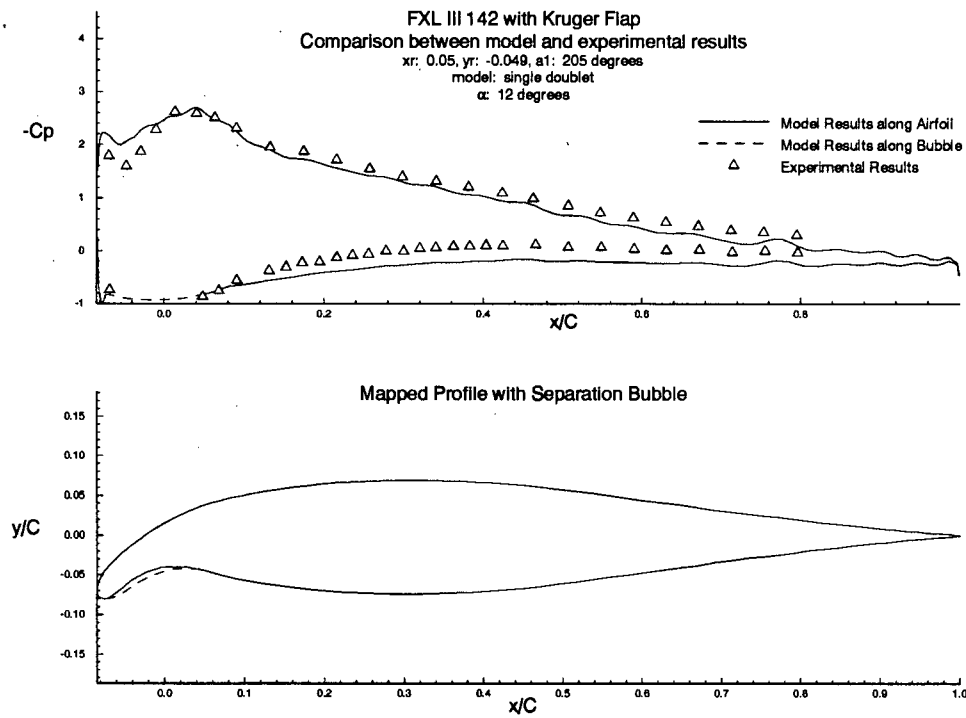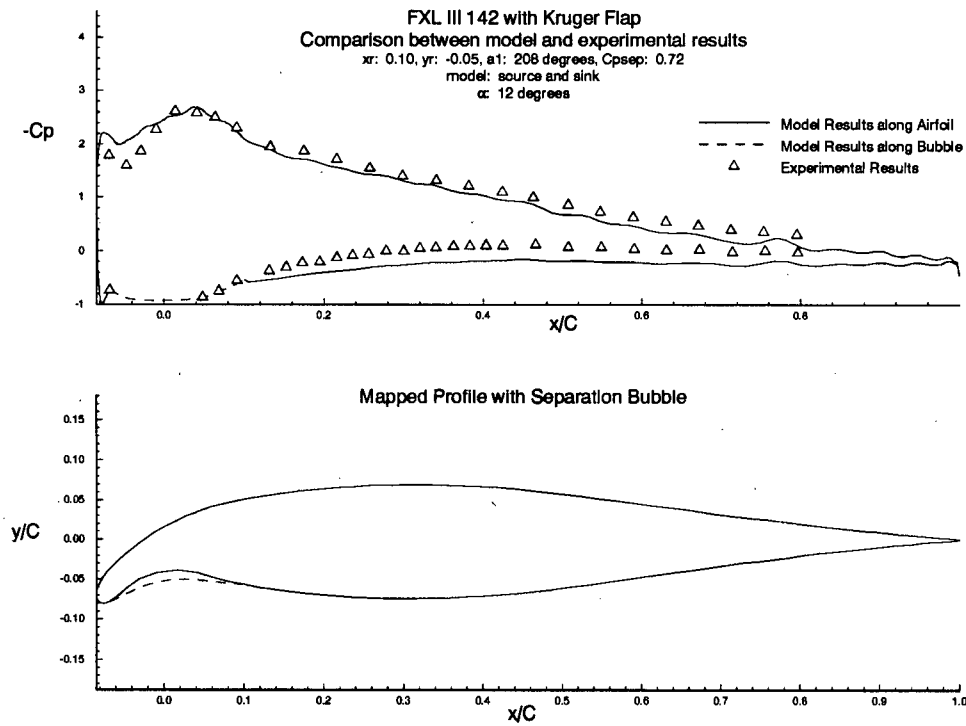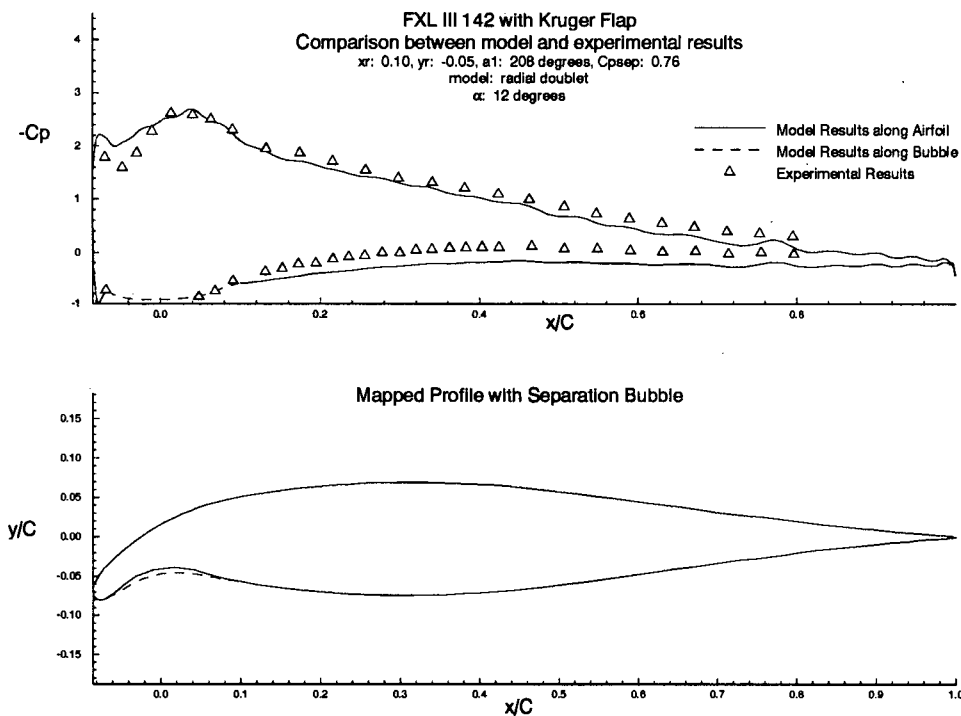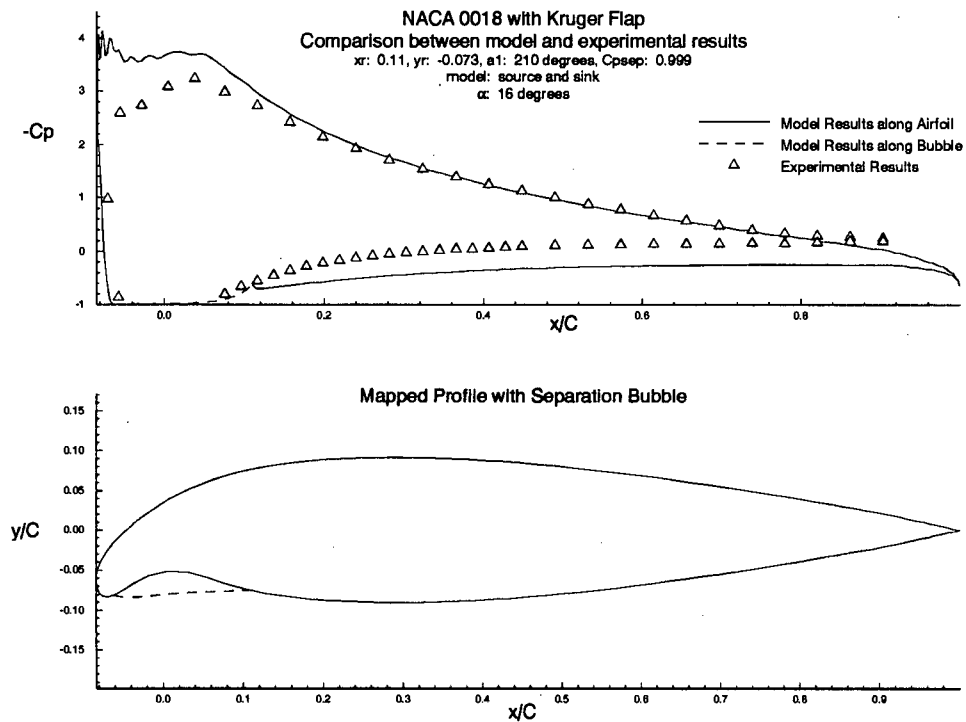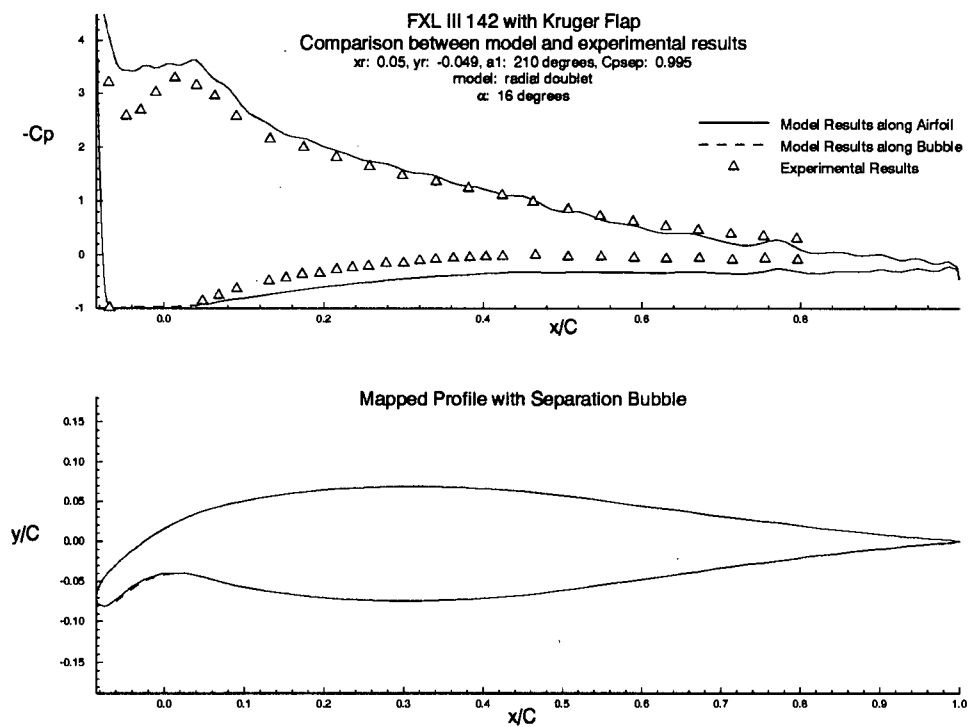
Figure 4.45: FXL III 142, 16 degrees, radial doublet model
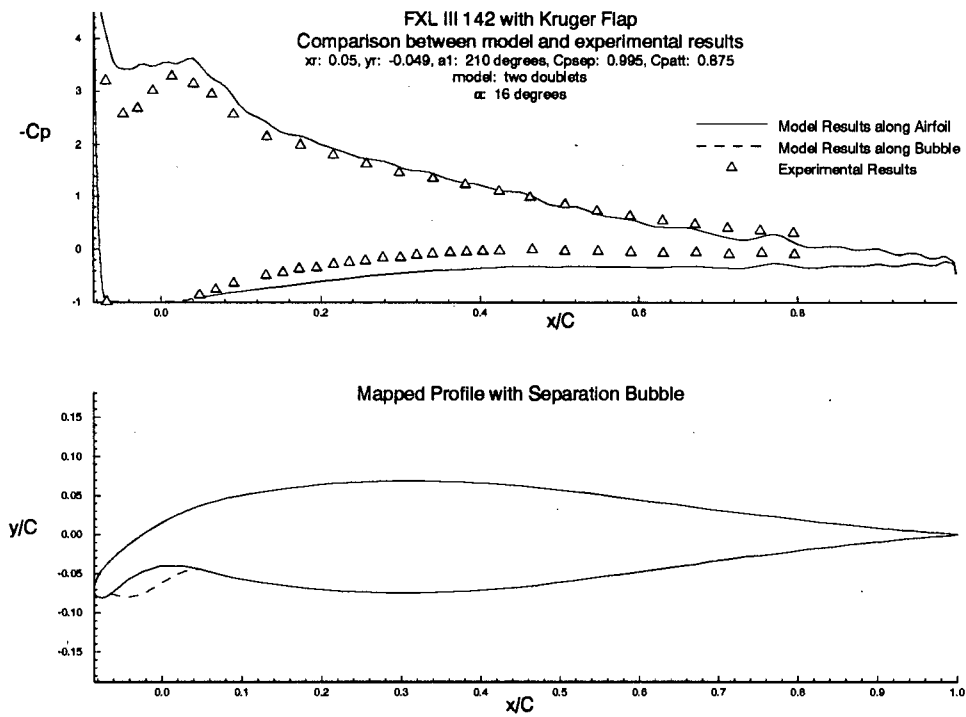
Figure 4.46: FXL III 142, 16 degrees, two doublets model
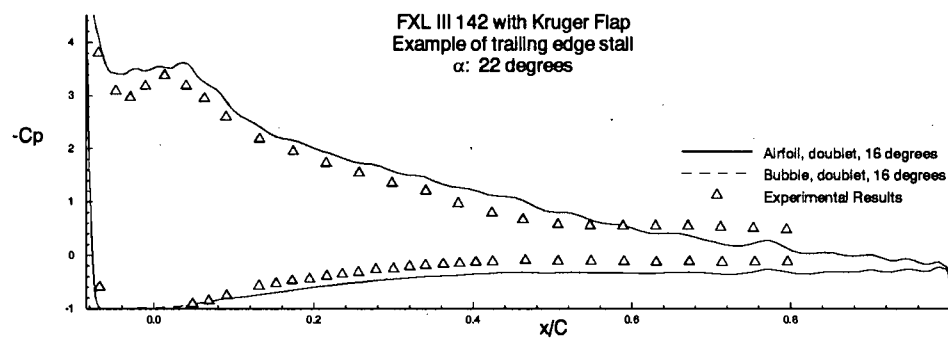
Figure 4.47: FXL III 142 at 22 degrees exhibiting trailing edge stall.

4.2.2   Oscillations in the Solution

There are a couple of additional points of interest about the numerical solution. Upon closer examination of the models' output, an oscillation can be seen in the pressure coefficient on the suction surface of both airfoils, especially near the flap. It seems logical that a smoothly curved airfoil should result in a smooth pressure distribution, which doesn't seem to be the case.

For the FXL airfoil, the oscillations, especially near the trailing edge, are partly due to the nature of the profile. This airfoil has an experimentally determined profile, which is defined by a set of x and y coordinates. These coordinates do not form a smooth curve, resulting in perturbations that are visible to the eye.

The NACA airfoil, on the other hand, is defined by a known polynomial, and therefore has a perfectly smooth curve. This indicates that the problem is not entirely due to the airfoils, but is instead partly a property of the mappings used. The only mapping that doesn't deal with the airfoil as a smooth curve is the Theodorsen transformation. This mapping picks a number of equally spaced points on the airfoil near circle, and maps only these points to a perfect circle. Mapping the entire airfoil would require an infinite number of Theodorsen coefficients, and so is not done. In areas of the airfoil profile where there is a high curvature, such as along the flap, the regions between the points chosen for the mapping may give rise to the oscillations in the pressure coefficient. If this is the case, the results from generating several different sets of coefficients by mapping different sets of points along the airfoil could be averaged, and the oscillations should disappear. Figure 4.48 shows the pressure distribution along the flap of the NACA airfoil at 12° for ten different sets of Theodorsen coefficients. The coefficients were generated for 10 equally spaced (in the near circle plane) sets of airfoil coordinates.

The results do seem to be oscillating about a mean. Unfortunately, when the average is taken, it becomes apparent that there is still a warble in the average, albeit smaller than originally. The question of how many sets of coefficients one must average to entirely remove the oscillation arises. Figure 4.49 attempts to answer that question by giving a comparison between the original ten equally spaced sets of coefficients and four new equally spaced sets of coefficients,
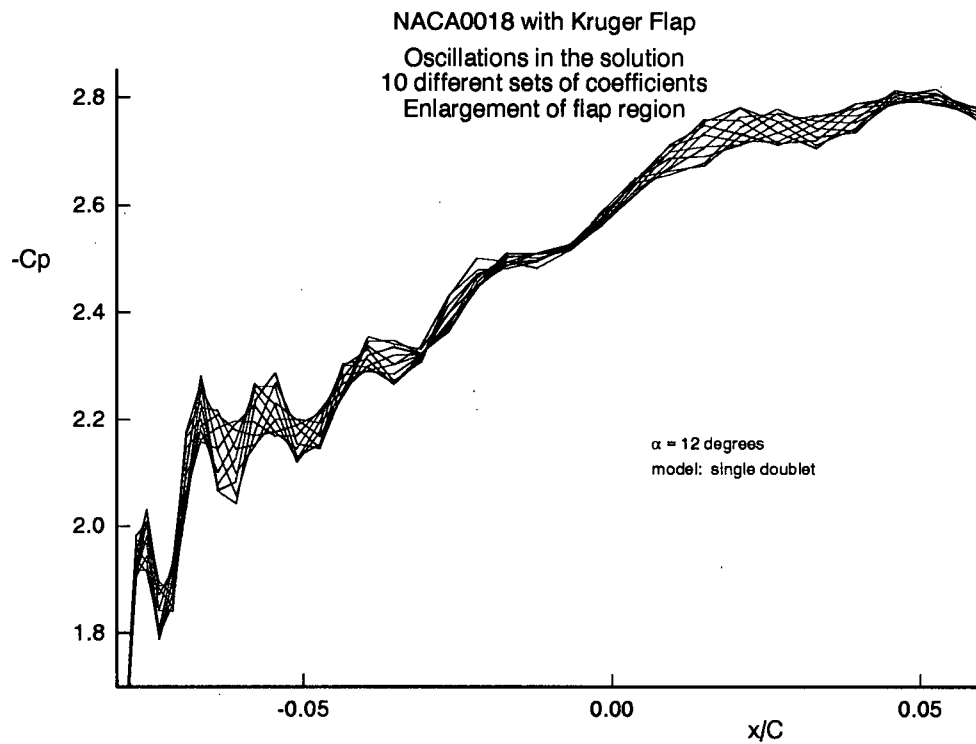
Figure 4.48: Pressure distribution in flap region for ten different sets of Theodorsen coefficients.

with no set of coefficients in common. The resulting averaged pressure distributions are virtually identical. There is no advantage in averaging more sets of coefficients. This last remnant of the warble appears to be a property of the mappings, and there doesn't seem to be an easy way of removing it. All of the model pressure distributions that have been presented are the result of an average of four sets of coefficients.
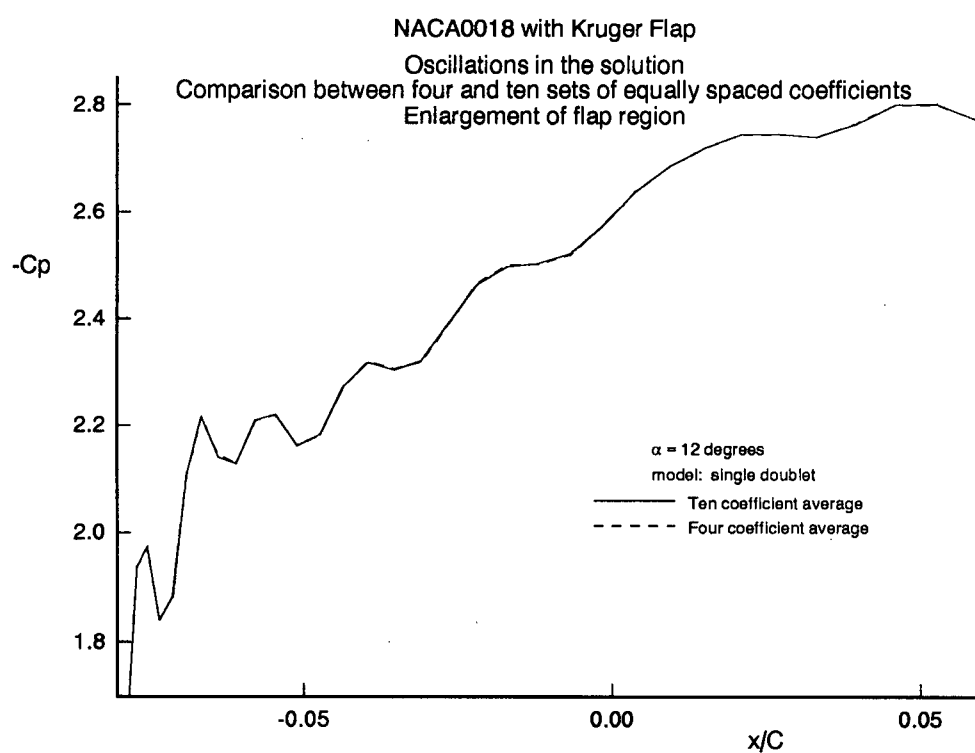
Figure 4.49: Comparison between the averages for four and ten sets of Theodorsen coefficients.

4.2.3 Boundary Layer Thickening of the Airfoils

All of the results from the models also differ a little from the experimental results near the trailing edge. The flow model predicts a higher pressure coefficient here than was found experimentally. This indicates that, experimentally, the air was moving faster in this region than it should have been according to the principles of ideal fluid flow. It was thought that this might be due to boundary layer thickening of the airfoil. The boundary layer would be small near the leading edge, but would thicken quickly as it encountered the adverse pressure gradient along the suction surface. As the boundary layer thickened, it would shift the streamlines farther away from the airfoil. The air would have to travel faster around this thickened airfoil, causing the lower pressure coefficients seen.

In view of this, the displacement thickness of a turbulent boundary layer was added to the original airfoil, and this new airfoil was run through the models. The boundary layer displacement thickness was calculated by Moses' method, as in references [4] and [9]. The pressure distribution calculated by the single doublet model along the original airfoil and flap was used to determine the free stream velocity and pressure gradients. The results for the FXL airfoil at 12° are shown in figure 4.50.

Along the suction surface, the addition of the boundary layer brought the predicted and measured pressures into excellent agreement. The lack of smoothness near the trailing edge is easily explained. For the airfoil to be properly mapped, the profile must still come to a cusp or wedge at the trailing edge, even with the boundary layer added. This means that the boundary layer must be arbitrarily brought back to zero thickness in some fashion. For this approximation, the boundary layer thickness was linearly reduced from a maximum thickness about two inches before the trailing edge to zero thickness at the trailing edge. This results in a less smooth pressure distribution near the trailing edge once the boundary layer is added.

On the pressure surface, the addition of the boundary layer has little effect on the pressure distribution. Good agreement is not to be expected, though, as the boundary layer here is not simply a laminar or turbulent boundary layer subject to a pressure gradient. The separation
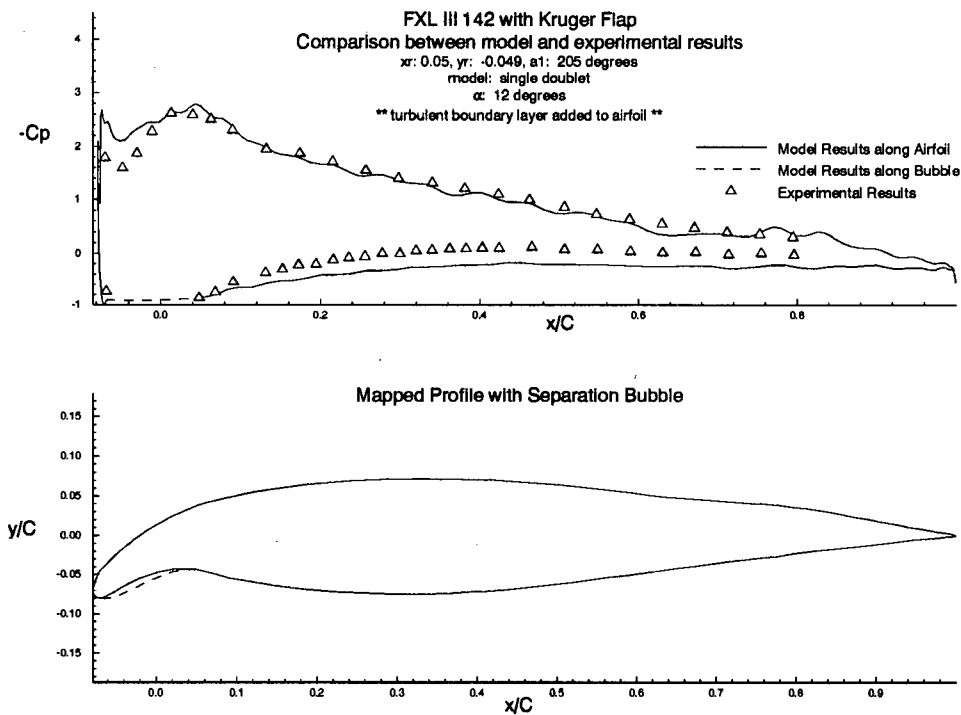
Figure 4.50: Effect on the pressure distribution of the addition of a turbulent boundary layer.

and reattachment of the free shear layer makes it difficult to determine a proper boundary layer thickness. Simply calculating a displacement thickness, as was done, probably underestimates the thickness.

4.2.4 Convergence Problems among the Models

While all of the models converged for the range of angles of attack studied, they would not all do so for given sets of boundary conditions. Often, different boundary conditions were needed for each model at a given angle of attack.

The single doublet model is the simplest approach, and also the most robust. It converges for all angles of attack up to about $20°$, independent of the initial guesses for the location of the doublet. It will also converge for a wide variety of separation and reattachment points, except at high angles of attack, when the separation point must be shifted slightly downstream.

All three of the models that use the separation pressure boundary condition often have difficulty converging for the experimentally determined pressure coefficient. Often this condition must be relaxed, which results in the similarity of results from the models at higher angles of attack.

The source and sink model was also well behaved, converging for only a slightly smaller range of initial inputs than the single doublet, especially if the separation pressure coefficient boundary condition is relaxed to allow a suction spike at separation. As noted in the discusion of the mid range angles of attack, this model does not always generate realistic pressure distributions. To match a low separation pressure coefficient, it will often create a suction spike on its own, as in figure 4.29, that matches the separation condition, but leaves the pressure along the bubble unchanged. The initial guesses for source and sink strength and location could speed or delay convergence, but this model will generally find a solution if one exists.

The radial doublet model was a pleasant surprise, as it was almost as robust at the single doublet. Initial guesses for the unknowns did not affect it very much at all, and it almost always satisfied, or came close to satisfying, the boundary conditions. At times, it generated solutions which used a suction spike, but not as often as the source and sink. In all cases, relaxing the boundary conditions removed the spike.

The two doublet model was not enjoyable to use. It has large convergence problems. Even slight changes in the Theodorsen coefficients will change the boundary conditions for which it converges, making averaging the results very difficult. This model will also not converge for as wide a range of angles of attack as the previous three models.

This model is very sensitive to the initial guesses for δ_1 and δ_2, the initial locations of the doublets. At times, selecting δ_1 close to separation, and δ_2 close to reattachment will result in convergence, while at other times, equally spacing the doublets, or placing both near the middle of the separation region works best. Even changing these initial guesses slightly may result in non-convergence.

If this model is to be used in the future, I strongly suggest that the time be taken to rewrite the portion of the code involving the non-linear solver.

Chapter 5

Conclusions

5.1 Summary of results

Four different variations of the potential flow model were studied over a wide range of angles of attack. The single doublet and two doublets variations had been previously developed by Brun, while the radial doublet and source and sink variations were created as part of this research. The results from these theoretical models were compared with experimental results for two different airfoil profiles.

The experimental results showed that the addition of a Kruger flap to the clean airfoil profile had the desired effect on the lift curve. The maximum lift coefficient for the NACA 0018 airfoil was increased by between 0.32 and 0.41, while delaying stall by 2°. The maximum lift coefficient for the FXL III 142 airfoil was increased by approximately 0.40, and stall was delayed by 5° or 6°. As expected, the most dramatic improvements in lift curve and stall angle were observed on the FXL airfoil, the airfoil with the smaller leading edge radius.

At small angles of attack, the theoretically predicted pressure distributions were not in close agreement with the experimental results. All four variations of the theoretical model predicted pressures along the bubble that were uniformly greater than measured values. Along the rest of the airfoil, agreement was also poor, as both the size and effects of the separation bubble were largest at small angles. This meant that the failure of the models to correctly predict the bubbles properties caused greater problems here than at larger angles of attack.

The different model variations gave different bubble shapes and pressure distributions, but very

similar results along the rest of the airfoils. Results from the single doublet and source and sink models were the poorest. The two doublet model offered slight improvements, and the radial doublet model performed the best.

Agreement between experimental and theoretical results improved as angle of attack increased. At the same time, the results from the different models converged, with each model giving similar results in the middle range of angles of attack, from 8° to 14°.

All models gave their best performance in this region, giving excellent results for the suction surface of the airfoils, and good results on the pressure surface, as well as along the separated region.

As the angle of attack is further increased, the models still perform well, until close to stall, where non-linear and viscous effects begin to play a larger role in determining the pressure distribution along the airfoil. Near stall, the discrepancy between the theoretical and experimental results is most obvious in the suction peak, which the models began to overpredict.

Apart from the separated region at low angles of attack, there are several identifiable areas where the theoretical models have problems in successfully predicting the pressure.

In the first small portion of the suction peak, the model tends to overpredict the local velocity. This is not a surprise, as this is a region of high velocity gradients in the free stream, suggesting that the effects of viscosity are being seen. There is no easy fix for this problem, as it is a direct result of the assumptions in the formulation of the theoretical solution. Any potential flow model is going to encounter problems here. This effect was largest on the NACA 0018, an airfoil whose lift curve was already showing the effect of viscous losses. The effect was much smaller on the FXL airfoil, which had a nearly ideal lift curve.

The models underpredicted the local velocities near the trailing edge of the airfoils. This effect appears to be the result of boundary layer thickening of the airfoil, and can be accounted for on the suction surface by artificially thickening the airfoil by the displacement thickness of a turbulent boundary layer subject to the predicted pressure gradient.

There was also a slight underprediction of the velocities along the pressure surface of the airfoil, which could not be corrected for by thickening the pressure surface of the airfoil in a manner similar to the method used on the suction surface. This underprediction could well be the result of the separation and reattachment of the shear layer in the bubble region. Separation bubbles normally reattach by entraining a sufficient quantity of fluid from the area of separated flow. This might cause the reattached boundary layer to be much thicker than would be calculated by simple growth in a favourable pressure gradient.

Finally, the small oscillations in the pressure distribution near the leading edge of the suction surface resulted, at least partly, from the pointwise nature of the Theodorsen transformation. By generating several slightly different sets of Theodorsen coefficients and averaging the results, the oscillations could be reduced, but not completely removed.

None of the models were very sensitive to the location of either the separation or reattachment points. As long as the separation point was chosen close to the tip of the Kruger flap, and the reattachment point was chosen sufficiently downstream of this point, the models remained fairly consistent in the pressure distributions that were predicted. The choice of separation and reattachment points did affect the convergence of the models, however, especially at higher angles of attack.

The shape of the separation streamline representing the bubble boundary was not consistent between models. Even for the same model at various angles of attack, the bubble shape did not seem to vary in any predictable way. This feature of the model was not closely examined, as no experimental measurements of the bubble shape were made.

In conclusion, while none of the models functioned remarkably well at low angles of attack, the radial doublet model did significantly outperform the other models, and should be chosen if results are needed at low angles.

At higher angles of attack, all models performed similarly. This suggests that the single doublet model, which was the simplest model, required the smallest number of inputs, and was the most robust, should be used. Alternatively, the radial doublet model, which is only slightly more

complicated and needs only one additional input, and was nearly as robust, could be used to provide consistency with the results from smaller angles of attack.

5.2 Recommendations for the future

Most of the research on this project seems to have been done, but two additional areas of research would be useful.

The results along the pressure surface of the airfoils indicate that the boundary layer here may be large. A study of the pressure surface boundary layer, and a simple method of prediction its thickness after reattachment could increase the accuracy of the model.

Additionally, flow visualization of the separation region would allow separation bubble location to be measured. These results would then be used to find the model with the most realistic bubble, as well as accurately determining separation and reattachment points.

Apart from these two minor points, the results obtained indicate that the theoretical models are working well in the range of angles where a Kruger flap is most likely to be used. The next logical step would be to use the models in a wing design situation.

Appendix A

Airfoil Profiles

NACA 0018 with Kruger Flap: Upper Surface

x	y	x	y	x	y
25.74200	0.000000	12.14345	2.887850	1.913545	2.140623
25.49602	0.073091	11.64632	2.950069	1.825052	2.088631
25.25000	0.145682	11.14892	3.007626	1.737009	2.035204
25.00394	0.217500	10.65120	3.060156	1.649422	1.980327
24.51171	0.359364	10.15315	3.107251	1.562294	1.923983
24.01933	0.498659	9.654740	3.148455	1.475633	1.866154
23.52645	0.630053	9.155935	3.183254	1.389443	1.806822
23.03309	0.753464	8.656701	3.211064	1.303731	1.745966
22.53959	0.874659	8.156997	3.231216	1.218505	1.683565
22.04596	0.993689	7.656774	3.242935	1.133770	1.619595
21.55220	1.110596	7.155978	3.245305	1.049165	1.555213
21.05831	1.225409	6.654540	3.237234	0.965570	1.487612
20.56429	1.338144	6.152379	3.217378	0.882636	1.417905
20.07014	1.448805	5.649390	3.184049	0.800433	1.345868
19.57587	1.557386	5.145439	3.135047	0.719047	1.271228
19.08146	1.663864	4.640341	3.067374	0.638583	1.193649
18.58693	1.768206	4.133830	2.976704	0.559173	1.112712
18.09226	1.870364	3.879925	2.920780	0.480986	1.027874
17.59746	1.970277	3.625492	2.856270	0.404249	0.938419
17.10251	2.067868	3.009300	2.656689	0.329269	0.843363
16.60741	2.163047	2.729628	2.545942	0.256490	0.741294
16.11216	2.255708	2.637242	2.506356	0.186593	0.630040
15.61675	2.345729	2.545278	2.465426	0.120723	0.505953
15.12116	2.432971	2.453738	2.423145	0.061112	0.361917
14.62540	2.517276	2.362624	2.379506	0.035123	0.277741
14.12944	2.598469	2.271938	2.334501	0.013524	0.179570
13.63328	2.676353	2.181684	2.288120	0.003301	0.100787
13.13691	2.750710	2.091865	2.240355	4.19E-10	1.18E-10
12.64030	2.821298	2.002484	2.191193		

NACA 0018 with Kruger Flap: Inverted Lower Surface

x	y	x	y
0.004487	0.069967	9.890081	1.176374
0.011057	0.118690	10.39015	1.190577
0.038616	0.234396	10.89055	1.199345
0.074592	0.308964	11.39127	1.203086
0.095826	0.336554	11.89226	1.202165
0.114524	0.356059	12.39353	1.196910
0.131861	0.371231	12.89504	1.187619
0.148300	0.383536	13.39679	1.174560
0.164076	0.393731	13.89875	1.157973
0.179332	0.402269	14.40091	1.138078
0.194161	0.409447	14.90327	1.115071
0.208628	0.415470	15.40580	1.089127
0.222779	0.420488	15.90851	1.060404
0.236651	0.424614	16.41138	1.029040
0.250271	0.427936	16.91440	0.995159
0.263659	0.430523	17.41757	0.958865
0.276834	0.432429	17.92088	0.920250
0.289809	0.433698	18.42433	0.879390
0.302596	0.434367	18.92792	0.836346
0.315204	0.434466	19.43164	0.791165
0.327640	0.434017	19.93548	0.743882
3.076469	-0.03413	20.43946	0.694518
3.442186	0.128524	20.94356	0.643081
3.931968	0.310255	21.44778	0.589566
4.423577	0.462223	21.95214	0.533957
4.916598	0.591193	22.45663	0.476224
5.410767	0.701493	22.96125	0.416327
5.905897	0.796120	23.46601	0.354213
6.401855	0.877273	23.97125	0.284117
6.898537	0.946643	24.22410	0.245368
7.395860	1.005570	24.47699	0.206100
7.893758	1.055149	24.72992	0.166074
8.392173	1.096294	24.98288	0.125554
8.891058	1.129782	25.23587	0.084384
9.390373	1.156281	25.48892	0.042442

Clean FXL III 142: One surface only
as airfoil is symmetrical

x	y	x	y
0.00000	0.0000	12.78576	1.3248
0.02448	0.1008	13.56600	1.2144
0.10128	0.2352	14.34000	1.1112
0.23040	0.3888	15.10512	0.9984
0.40848	0.5376	15.85776	0.9072
0.63600	0.6768	16.59192	0.8016
0.91248	0.8016	17.31720	0.7008
1.23792	0.9312	17.99880	0.6240
1.60656	1.0464	18.66552	0.5616
2.02128	1.1616	19.30440	0.4608
2.47920	1.2576	19.91280	0.3888
2.97672	1.3488	20.48400	0.3312
3.51432	1.4304	21.02160	0.2736
4.08888	1.5072	21.51456	0.2304
4.69392	1.5744	21.97704	0.1824
5.33304	1.6272	22.39176	0.1392
5.99952	1.6656	22.76352	0.1152
6.69384	1.6944	23.08608	0.0816
7.40664	1.704	23.36256	0.0624
8.14392	1.6992	23.58984	0.0480
8.89344	1.6752	23.76816	0.0336
9.65832	1.6368	23.89704	0.0192
10.4326	1.584	23.97384	0.0144
11.2159	1.512	24.00000	0.0000
11.9998	1.416		

FXL III 142 with Kruger flap: upper surface

x	y	x	y
25.87232	0.000000	8.701510	2.745460
25.64295	0.047660	8.006725	2.759008
25.46584	0.072896	7.339144	2.761278
25.23986	0.101114	6.697994	2.747508
24.96506	0.137120	6.089984	2.717289
24.64515	0.190306	5.511813	2.675631
24.27554	0.236908	4.970241	2.626931
23.86422	0.305290	4.468089	2.566206
23.40553	0.381373	4.005172	2.498279
22.91611	0.454521	3.584204	2.408556
22.38302	0.544762	3.209231	2.316025
21.81639	0.637050	2.876501	2.206490
21.21351	0.745977	2.592932	2.098764
20.58195	0.885508	2.518869	2.068366
19.92027	0.988405	2.374655	2.006406
19.24462	1.106582	2.154737	1.904667
18.52682	1.251375	1.937213	1.795055
17.80046	1.401501	1.722124	1.677430
17.05477	1.538379	1.509523	1.551620
16.29794	1.697576	1.299472	1.417419
15.53167	1.847733	1.092047	1.274581
14.75960	2.005456	0.919495	1.147401
13.98014	2.144396	0.645812	0.928758
13.20408	2.287936	0.417576	0.728946
12.42656	2.407521	0.240372	0.529595
11.65698	2.507385	0.113263	0.335438
10.89586	2.592307	0.034394	0.150926
10.14919	2.661919	0.000000	4.23E-12
9.413571	2.711622		

FXL III 142 with Kruger flap: inverted lower surface

x	y	x	y
0.005893	0.103560	12.23358	0.75460
0.057898	0.192130	13.01987	0.73045
0.091687	0.220770	13.80763	0.68235
0.122090	0.238270	14.59820	0.63922
0.150557	0.249400	15.38372	0.57656
0.177654	0.256020	16.16257	0.52070
0.203663	0.259060	16.93314	0.45471
0.252995	0.256310	17.68994	0.40953
0.276461	0.250980	18.42916	0.34885
0.299161	0.243140	19.15924	0.29242
3.095783	-0.45708	19.84425	0.25728
3.456721	-0.31964	20.51353	0.23561
3.863654	-0.17939	21.15737	0.17391
4.314875	-0.05568	21.76902	0.13911
4.805916	0.065660	22.34267	0.11641
5.337547	0.179860	22.88278	0.09166
5.906362	0.291510	23.37746	0.07857
6.506185	0.395440	23.84200	0.05883
7.140901	0.487080	24.25858	0.04098
7.803805	0.566010	24.63112	0.03967
8.495081	0.637050	24.95512	0.02578
9.205972	0.690050	25.23226	0.02345
9.942176	0.730170	25.45999	0.02293
10.69177	0.751870	25.63886	0.01942
11.45756	0.760140		

Bibliography

[1] Brun, S. (1993)
"A Potential Flow Model for Separated Flow around Airfoils"
M.A.Sc Thesis, The University of British Columbia

[2] Fullmer, F.F. Junior (1947)
"Two-Dimensional Wind-Tunnel Investigation of the NACA 64_1-012 Airfoil Equipped with Two Types of Leading Edge Flap"
NACA TN no. 1277

[3] Hameury, M. (1987)
"Development of the Tolerant Wind Tunnel for Bluff Body Testing"
Ph.D Thesis, The University of British Columbia

[4] Hill, P., and Peterson, C. (1992)
"Mechanics and Thermodynamics of Propulsion", 2nd ed.
Addison-Wesley Publishing, 1992

[5] Kruger, W. (1947)
"Systematic Wind-Tunnel Measurements on a Laminar Wing with Nose Flap"
NACA TM no. 1119

[6] Kruger, W. (1947)
"Wind-Tunnel Investigations on a Changed Mustang Profile with Nose Flap"
NACA TM no. 1177

[7] Jandali, T. (1970)
"A Potential Flow Theory for Airfoil Spoilers"
Ph.D Thesis, The University of British Columbia

[8] Miley, S.J. (1982)
"A Catalog of Low Reynolds Number Airfoil Data for Wind Tunnel Applications"

[9] Moses, H.L. (1968)
"A Strip-Integral Method for Predicting the Behaviour of Turbulent Boundary Layers"
Proc. AFOSR-IFP-Stanford Conference on Computation of Turbulent Boundary Layers
Stanford University, Palo Alto, Calif.

[10] Parkinson, G.V., and Hameury, M. (1988)
"Performance of the Tolerant Tunnel for Bluff Body Testing"
J. of Wind Engineering, No. 37, October 1988, pp 11-18

[11] Parkinson, G.V., and Jandali, T. (1970)
"A Wake Source Model for Bluff Body Potential Flow"
Journal of Fluid Mechanics, Vol. 40, no. 3, pp 577-594

[12] Parkinson, G.V., and Yeung, W. (1987)
     "A Wake Source Model for Airfoils with Separated Flow"
     Journal of Fluid Mechanics, Vol. 179, pp 41-57

[13] Roshko, A. (1954)
     "A New Hodograph for Free-Streamline Theory"
     NACA TN no. 3168

[14] Roshko, A. (1954)
     "On the Drag and Shedding Frequency of Two-Dimensional Bluff Bodies"
     NACA TN no. 3169

[15] Theodorsen, T (1932)
     "Theory of Wing Sections of Arbitrary Shape"
     NACA TR no. 411

[16] Williams, C. (1975)
     "A New Slotted Wall Method for Producing Low Boundary Corrections in Two Dimensional Airfoil Testing"
     Ph.D. Thesis, The University of British Columbia

[17] Woods, L.C. (1955)
     "Two-dimensional flow of a compressible fluid past given curved obstacles with infinite wakes"
     Proceedings of the Royal Society of London, A227, pp 367-386